



Contents lists available at ScienceDirect

International Journal of Plasticity

journal homepage: www.elsevier.com/locate/ijplas

A virtual laboratory using high resolution crystal plasticity simulations to determine the initial yield surface for sheet metal forming operations



Haiming Zhang ^{a, b, *}, Martin Diehl ^a, Franz Roters ^{a, **}, Dierk Raabe ^a

^a Max-Planck-Institut für Eisenforschung, Max-Planck-Str. 1, 40237 Düsseldorf, Germany

^b Institute of Forming Technology & Equipment, Shanghai Jiao Tong University, 1954 Hua Shan Road, Shanghai 200030, China

ARTICLE INFO

Article history:

Received 21 July 2015

Received in revised form 7 January 2016

Available online 26 January 2016

Keywords:

A. Yield condition
A. Cutting and forming
B. Anisotropic material
B. Crystal plasticity
Spectral methods

ABSTRACT

We present a virtual laboratory to investigate the anisotropic yield behavior of polycrystalline materials by using high resolution crystal plasticity simulations. Employing a fast spectral method solver enables us to conduct a large number of full-field virtual experiments with different stress states to accurately identify the yield surface of the probed materials. Based on the simulated yield stress points, the parameters for many commonly used yield functions are acquired simultaneously with a nonlinear least square fitting procedure. Exemplarily, the parameters of four yield functions frequently used in sheet metal forming, namely Yld91, Yld2000-2D, Yld2004-18p, and Yld2004-27p are adjusted to accurately describe the yield behavior of an AA3014 aluminum alloy at two material states, namely with a recrystallization texture and a cold rolling texture. The comparison to experimental results proves that the methodology presented, combining accuracy with efficiency, is a promising micromechanics-based tool for probing the mechanical anisotropy of polycrystalline metals and for identifying the parameters of advanced yield functions.

© 2016 Elsevier Ltd. All rights reserved.

1. Introduction

Because of their complex thermo-mechanical treatments, polycrystalline metals are generally crystallographically textured, and therefore their mechanical properties are anisotropic. The directionality of the mechanical properties must be taken into account when modeling metal forming operations. The anisotropy induced by plastic strain during forming operations is small compared to that induced by the thermo-mechanical treatment and negligible for most applications (Yoon et al., 2006). Crystal plasticity (CP) models which use the crystallographic texture and the intrinsic single crystalline anisotropy as input can accurately describe the anisotropic behavior of polycrystalline materials and naturally consider the stress and strain partitioning among different phases, grains, and subgrains (Roters et al., 2010). However, the long computation times required to integrate the underlying constitutive equations render their use infeasible for engineering simulations of large scale components. Due to their high efficiency and straightforward implementation, analytical yield functions are thus used instead of full-field CP simulations at the engineering scale to describe the anisotropy of materials.

* Corresponding author. Current address: Institute of Forming Technology & Equipment, Shanghai Jiao Tong University, 1954 Hua Shan Road, Shanghai 200030, China. Tel.: +86 21 62933955; fax: +86 21 62933955.

** Corresponding author. Tel.: +49 211 6792393.

E-mail addresses: hm.zhang@sjtu.edu.cn (H. Zhang), f.roters@mpie.de (F. Roters).

Starting with the first anisotropic yield function proposed by von Mises (1928), various yield functions have been established to describe the flow behavior of different material classes. The quadratic anisotropic yield function developed by Hill (1948) was validated by numerous experiments and is well suited for body centered cubic (bcc) materials, especially for steels (Hill, 1990). However, it can not accurately describe the yield behavior of face centered cubic (fcc) metals, e.g., aluminum alloys (Hosford, 1988), as only higher order ansatz functions are capable of predicting the rather angular form of yield surfaces and the so-called “anomalous behavior” (Darrieulat and Piot, 1996), i.e., the experimental observation that the equi-biaxial yield stress is higher than the uniaxial yield stress while the r -value is below 1.0 (Woodthorpe and Pearce, 1970). To overcome these limitations, Hill (1979) and Hosford (1985) proposed non-quadratic anisotropic yield functions. Later, Barlat and Lian (1989), Barlat et al. (1991, 1997, 2003, 2005), Karafillis and Boyce (1993), Banabic et al. (2003), Bron and Besson (2004) introduced further improved formulations, where linear transformations of the stress tensor are used to describe the anisotropy (Barlat et al., 2007).

For material models used in a commercial context, it is preferable that only a small set of simple and low-cost tests, e.g., uniaxial tensile tests, are necessary for calibration (Lademo et al., 1999). The ability of advanced yield functions to describe the mechanical anisotropy of various material classes, however, comes at the price of requiring many parameters. Improved flexibility and accuracy therefore makes the parameter identification process more challenging as more experimental results are needed. These experiments are expensive, time consuming, and sometimes very difficult to perform, e.g., when out-of-plane properties of sheet metals are required. Additionally, since no standards are defined for most of these experiments, evaluation of a parameter set requires an in-depth knowledge about the details of the fitting procedure that was employed to retrieve it.

Besides considering experimental results, numerical models are frequently used to examine the mechanical response of polycrystalline materials. Micromechanical models based on CP theory play a significant role in understanding yielding and anisotropy of metals, as well as in evaluating yield surface models. The earliest of such approaches, proposed by Sachs (1929), uses an iso-stress approach and assumes the same resolved stress on the slip systems with the highest resolved shear stress in all grains within the polycrystalline aggregate. In contrast, the full-constraint (FC) model developed by Taylor (1938) is based on the iso-strain assumption, i.e., all grains within an aggregate experience the same state of deformation. The FC TAYLOR model was elaborated further by Bishop and Hill (1951), and was used as the TAYLOR–BISHOP–HILL (TBH) model by many researchers to validate yield functions (Hosford, 1972; Barlat and Lian, 1989; Barlat et al., 1997) or to generate the analytical expressions for plastic potentials and yield surfaces of anisotropic polycrystalline materials (Gambin, 1991; Van Houtte, 1994, 2001; Li et al., 2003; Van Houtte and Van Bael, 2004; Kowalczyk and Gambin, 2004; Van Houtte et al., 2009). It should be noted that the SACHS model satisfies the stress equilibrium condition across the grains but violates the compatibility condition between them, while, in contrast, the TBH model violates the stress equilibrium condition but satisfies the compatibility condition among differently oriented grains (Kocks, 1958). The deformation behavior of real polycrystals, where both, compatibility and equilibrium are fulfilled, is in-between these two extremes (Sachtler et al., 2002). The former model therefore sets the lower bound and the latter is the upper bound of the observed behavior.

Although the TAYLOR model shows good performance in the prediction of deformation textures, it is not fully realistic due to the violation of stress equilibrium. Various relaxed-constraint (RC) TAYLOR models were developed relieving the rigid deformation constraint in TAYLOR's iso-strain hypothesis (Honneff and Mecking, 1981; Kocks and Chandra, 1982; Raphanel and Van Houtte, 1985; Hölscher et al., 1991, 1994; Raabe, 1995c). Also, a number of grain cluster models were introduced such as the LAMEL model, the advanced LAMEL (ALAMEL) model (Van Houtte et al., 1999, 2002, 2005), the grain interaction (GIA) model (Raabe, 1995a,b; Raabe et al., 2002b; Crumbach et al., 2006), and the relaxed grain cluster (RGC) model (Tjahjanto et al., 2010).

Another important class of homogenization schemes is based on the self consistent (SC) approach which was originally proposed by Kröner (1958) for the elastic case and later extended to the elastoplastic (Hill, 1965) and viscoplastic (Hutchinson, 1976) cases. In the SC theory, each grain within a polycrystalline aggregate is considered to be an ellipsoidal inclusion embedded in the surrounding homogeneous equivalent medium (HEM). Such models satisfy the stress equilibrium and the deformation compatibility simultaneously as they allow for different deformation responses in each grain depending on the relative stiffness between the grain and the HEM. Among the various SC models, the visco-plastic self consistent (VPSC) model developed by Molinari et al. (1987) and extended by Lebensohn and Tomé (1993, 1994) has been widely used to simulate plastic behavior and texture evolution of polycrystalline materials (Lebensohn et al., 1996, 1998; Segurado et al., 2012; Knezevic et al., 2013). Although the SC models relieve the drawbacks associated with the TAYLOR type models, further microstructural aspects of the deformation, such as local grain interaction and intra-grain inhomogeneities of the micro-mechanical fields, are not accessible to these models (Zhao et al., 2007; Lebensohn et al., 2012).

Recently, full-field CP models, which are capable of incorporating additional morphological information beyond crystallographic texture, either employing the finite element method (FEM, CPFEM) (Raabe et al., 2001; Raabe and Roters, 2004; Dawson et al., 2005; Zhao et al., 2008; Kanjarla et al., 2010; Roters et al., 2010; Van Houtte et al., 2011; Zhang et al., 2015a) or a spectral method using fast FOURIER transformation (FFT) (Lebensohn et al., 2012; Kanjarla et al., 2012; Eisenlohr et al., 2013; Tasan et al., 2014a; Shanthraj et al., 2015) based solvers have become computationally feasible for the simulation of representative volume elements (RVEs). The merits of such full-field approaches include: (i) fulfillment of both, stress equilibrium and strain compatibility at grain boundaries; (ii) representation of a real grain morphology as long as the discretisation is fine enough; (iii) consideration of the local grain interactions and intra-grain inhomogeneities associated with plastic deformation. The main drawback of the full-field CPFEM is the computational cost associated with the large number of material points needed for the simulation of a sufficiently highly resolved polycrystalline RVE. Compared with their FEM counterparts,

spectral methods using FFT show much higher efficiency in solving boundary value problems (BVPs) (Prakash and Lebensohn, 2009; Lebensohn et al., 2012; Eisenlohr et al., 2013), at the cost of being limited to periodic boundary conditions (BCs). The spectral method was successfully used in simulating crystallographic texture evolution (Liu et al., 2010), modeling micro-mechanical response of two-phase materials (Lee et al., 2011), predicting internal lattice strain distributions in stainless steel (Kanjara et al., 2012), the local stress partitioning of dual-phase steel (Tasan et al., 2014b).

Virtual laboratory approaches, using fine-scale full-field modeling, e.g., CP models for the calibration of yield loci and the identification routines required for acquiring the parameters of advanced phenomenological yield functions, enable us to combine advantages of both methods, i.e., the accuracy of CP models and the computational efficiency of analytic yield functions (Raabe, 2000; Kraska et al., 2009; Van Houtte et al., 2009; Lademo et al., 2009; Helm et al., 2011). In such a scheme, virtual tests are performed using a CP model to provide yield stress points for the parameter identification of yield functions. Unlike mechanical experiments, which are limited to certain accessible deformation modes, the virtual CP tests are able to provide data for any deformation modes, which renders the approach especially attractive for identifying for instance the out-of-plane mechanical response of sheet metal materials. Barlat and Chung (2005) adopted the TBH model to generate the flow surfaces based on crystallographic texture measurements. Barlat et al. (2005) used the flow stress curves predicted by a VPSC model under different applied BCs to evaluate the out-of-plane properties of a 2090-T3 Al–Li alloy sheet, where the complete parameter set of the Yld2004-18p yield function was identified by a combination of results from experiments and VPSC simulations. Plunkett et al. (2006) used the VPSC model to identify the parameters of yield function developed by Cazacu et al. (2006) and simulated the change of anisotropy parameters associated with the twinning induced texture evolution in zirconium. Grytten et al. (2008) evaluated different parameter identification methods for the Yld2004-18p yield function, i.e., different combinations of mechanical experimental data and virtual test data obtained by using the FC_{TAYLOR} model. Even though both, mechanical and virtual test results could be satisfactorily reproduced by the adjusted yield function, the authors suggested that more advanced CP models are needed because the FC_{TAYLOR} model lacks the ability to quantitatively reproduce the mechanical experiments. Rabahallah et al. (2009) adopted a texture based procedure to identify the parameters of the plastic strain rate potential Srp2004-18p. More recently, Zhang et al. (2015b) investigated the anisotropy of an AA1050 aluminum sheet by using different CP models, including the FC_{TAYLOR} model, the ALAMEL model, the ALAMEL Type III model, the VPSC model, and a CPFEM approach. Employing various calibration methods corresponding to different combinations of uniaxial tensile data and virtual yield stress points, the authors identified the parameters of the Yld2004-18p yield function and concluded that the FC_{TAYLOR}, VPSC, and ALAMEL models are not capable of capturing the plastic anisotropy of the AA1050 aluminum sheet. These CP models were also employed to predict the plastic anisotropy of AA3103 sheets in the cold-rolled and fully annealed conditions (Zhang et al., 2014). Gawad et al. (2015) adopted an ALAMEL CP model as the basic constituent of the virtual laboratory to calculate the data for the identification of the BBC2008 yield function parameters.

Due to the crucial role of the initial crystallographic texture, the success of a virtual laboratory approach critically depends on the accurate and representative characterization and representation of the underlying microstructure. Full-field CPFEM models are able to use arbitrary complex microstructures and they do account for grain-to-grain interactions and intra-granular field variations (Beaudoin et al., 1995, 1996; Raabe et al., 2003). However, the large number of degrees of freedom and elements required by CPFEM simulations to properly account for all relevant fine-scale microstructure features with a sufficient level of fidelity renders the calculation times often unaffordable. Its high numerical efficiency as compared to CPFEM makes the spectral integration method in conjunction with CP constitutive equations thus a promising alternative candidate, since it combines accuracy of the CPFEM approach with affordable computation times. This especially holds as the required periodic BCs are applicable to the case of RVE simulations. Therefore, the use of spectral solvers in conjunction with CP constitutive models provides quantitative microscopic mechanical insights on the plastic anisotropy of metallic polycrystals at affordable computational costs.

This work aims to introduce a full-field CP based virtual laboratory which is able to probe the anisotropic properties of metals and further relieve the parameter identification of advanced yield functions. An efficient spectral solver in conjunction with a CP model (Roters et al., 2012; DAMASK, 2014) is used to perform full-field virtual experiments on highly resolved¹ microstructures. The anisotropic behavior of an AA3104 aluminum alloy with two different initial crystallographic textures and grain morphologies is investigated and the parameters of four widely used yield functions, namely, Yld91 (Barlat et al., 1991), Yld2000-2D (Barlat et al., 2003), Yld2004-18p (Barlat et al., 2005), and Yld2004-27p (Aretz et al., 2010) are determined. The methodology includes: mapping of the microstructure obtained from material characterization of the desired materials to a high resolution RVE; applying a large number of arbitrary BCs on the RVE to obtain yield stress points; and identifying the parameters of the yield functions using these stress probing points.

The presented work is structured as follows: Section 2 provides a concise background of the CP model and of the spectral method. In Section 3, we discuss the micromechanical meaning of the yield surface and present empirical yield functions that allow for an analytical description of plastic yielding. Section 4 introduces the set-up of the virtual laboratory. The details of the set-up for investigating the model systems are given in Section 5. The results are discussed and analysed in Section 6. The study ends with a conclusion and an outlook for further work in Section 7.

¹ With the term “highly resolved” we refer to an approach here where a set of integration points (Fourier points in the case of the spectral method) is used to represent grain morphologies in a RVE that substantially exceeds the number of crystals.

2. Crystal plasticity constitutive model and the spectral integration method

2.1. Finite strain crystal plasticity constitutive model

First we define a deformation map $\chi(\mathbf{x}) : \mathbf{x} \in \mathcal{B}_0 \rightarrow \mathbf{y} \in \mathcal{B}$, which projects material points \mathbf{x} in the reference configuration \mathcal{B}_0 to points \mathbf{y} in the current configuration \mathcal{B} . The deformation gradient, given by $\mathbf{F} = \partial\chi/\partial\mathbf{x}$, is then multiplicatively decomposed into elastic and plastic components as

$$\mathbf{F} = \mathbf{F}_e \mathbf{F}_p \quad (1)$$

where \mathbf{F}_p denotes the inelastic shear deformation in crystalline slip planes and slip directions, and \mathbf{F}_e contains the rotation and elastic distortion of the lattice. The plastic part of the velocity gradient, \mathbf{L}_p , is due to crystallographic slip on N slip systems and is expressed as

$$\mathbf{L}_p = \dot{\mathbf{F}}_p \mathbf{F}_p^{-1} = \sum_{\alpha} \dot{\gamma}^{\alpha} \mathbf{S}_0^{\alpha}, \quad \mathbf{S}_0^{\alpha} = \mathbf{s}_0^{\alpha} \otimes \mathbf{n}_0^{\alpha} \quad (2)$$

where $\dot{\gamma}^{\alpha}$ is the slip rate of slip system α , \mathbf{s}_0^{α} and \mathbf{n}_0^{α} are unit vectors defined in the crystal coordinate system representing the slip direction and the slip plane normal, respectively, constituting the SCHMID tensor \mathbf{S}_0^{α} .

Plastic flow results from dislocation movement under an applied resolved shear stress (RSS) τ^{α} . In this work, a rate dependent flow law is used to describe the plastic flow as

$$\dot{\gamma}^{\alpha} = \dot{\gamma}_0 \left| \frac{\tau^{\alpha}}{g^{\alpha}} \right|^{1/m} \text{sgn}(\tau^{\alpha}), \quad (3)$$

where $\dot{\gamma}_0$ is the reference slip rate, m determines the rate sensitivity of slip and g^{α} is the slip resistance, which evolves asymptotically from g_0 towards g_{∞} (Brown et al., 1989). The evolution equation of g^{α} has the following form:

$$\dot{g}^{\alpha} = \sum_{\beta} h^{\alpha\beta} \dot{\gamma}^{\beta} \quad (4)$$

with the instantaneous strain hardening matrix, $h^{\alpha\beta}$, which can be described phenomenologically by a saturation-type law as

$$h^{\alpha\beta} = h_0 [q + (1 - q)\delta^{\alpha\beta}] |1 - g^{\beta}/g_{\infty}|^a \text{sgn}(1 - g^{\beta}/g_{\infty}), \quad (5)$$

where h_0 , g_{∞} , and a are material parameters, representing the reference self-hardening coefficient, the saturation values of the slip resistance and the hardening exponent, respectively. The latent hardening parameter, q , is set to $q = 1.0$ for coplanar slip systems and $q = 1.4$ for non-coplanar slip systems (Peirce et al., 1982).

The RSS τ^{α} in Eq. (3) can be related to the externally imposed stress tensor as

$$\tau^{\alpha} = \boldsymbol{\sigma} : (\mathbf{F}_e \mathbf{S}_0^{\alpha} \mathbf{F}_e^{-1}) = (\mathbf{F}_e^T \mathbf{F}_e \mathbf{S}) : \mathbf{S}_0^{\alpha}, \quad (6)$$

where $\boldsymbol{\sigma}$ and \mathbf{S} are the CAUCHY stress tensor and the 2nd PIOLA-KIRCHHOFF stress tensor, respectively. With the assumption of small elastic strains, \mathbf{S} can be calculated by using the elastic GREEN strain tensor \mathbf{E}_e as

$$\mathbf{S} = \mathbf{C} : \mathbf{E}_e, \quad \mathbf{E}_e = (\mathbf{F}_e^T \mathbf{F}_e - \mathbf{I})/2, \quad (7)$$

where \mathbf{C} is the fourth order anisotropic elastic tensor. For cubic crystals, it can be specified in terms of three elastic constants C_{11} , C_{12} , and C_{44} .

2.2. Spectral method for integrating CP constitutive equations using FFT

The spectral method provides a solution of the governing equations such that the final equilibrated stress and compatible strain fields fulfil the required constitutive law at each material point. It usually exceeds the results obtained by corresponding FEM simulations in terms of the solution fidelity because its ansatz functions are trigonometric polynomials. Moreover, since it operates in FOURIER space, the use of FFT allows for a very time- and memory-efficient iterative solution algorithm. The spectral method presented here, which is based on a direct variational formulation, was firstly introduced by Moulinec and Suquet (1994) to calculate the micromechanical response of elastic composite materials and was later generalised to rigid-viscoplastic (Lebensohn, 2001) and elasto-viscoplastic (Lebensohn et al., 2012) materials. Eisenlohr et al. (2013) developed a further extension to the case of finite strain and general constitutive descriptions.

However, simulation of heterogenous materials is limited by the slow convergence of the original fixpoint iterative method when applied to materials with a large contrast in local stiffness (Michel et al., 2001). Several approaches have been proposed to overcome this limitation. Eyre and Milton (1999) and Monchiet and Bonnet (2012) introduced accelerated schemes for materials with large property contrast. Michel et al. (2001) suggested a method based on augmented LAGRANGIANS for materials with infinite property contrasts. Improved convergence can also be obtained via the use of advanced solution methods compared to the original approach (Zeman et al., 2010; Brisard and Dormieux, 2010). In Shanthraj et al. (2015), we recently benchmarked direct and mixed formulations in combination with various non-linear solution methods in a finite strain CP framework. The solution approach which shows the best performance is used within this work and is briefly recapitulated in the following.

2.2.1. Kinematics

The deformation map $\chi(\mathbf{x})$ introduced in Section 2.1, is expressed as a sum of a homogeneous deformation, characterized by a constant deformation gradient $\bar{\mathbf{F}}$, and a superimposed displacement fluctuation field $\tilde{\mathbf{w}}$,

$$\chi(\mathbf{x}) = \bar{\mathbf{F}}\mathbf{x} + \tilde{\mathbf{w}}(\mathbf{x}), \quad (8)$$

for which the periodicity conditions hold, *i.e.*, $\tilde{\mathbf{w}}^- = \tilde{\mathbf{w}}^+$ on corresponding surfaces $\partial\mathcal{B}^-$ and $\partial\mathcal{B}^+$. Eq. (8) allows to write the deformation gradient \mathbf{F} as the sum of the spatially homogeneous part, $\bar{\mathbf{F}}$, and the locally fluctuating part, $\tilde{\mathbf{F}} (= \partial\tilde{\mathbf{w}}/\partial\mathbf{x})$, *i.e.*, $\mathbf{F} = \bar{\mathbf{F}} + \tilde{\mathbf{F}}$.

The material response is governed by a constitutive law, *e.g.*, finite strain CP model, which relates the deformation gradient to the first PIOLA–KIRCHHOFF stress at every material point, \mathbf{P} , through a strain energy density functional, \mathcal{W} :

$$\mathbf{P}(\mathbf{x}) = \frac{\delta \mathcal{W}}{\delta \mathbf{F}(\mathbf{x})} = \mathbf{f}(\mathbf{x}, \mathbf{F}, \xi, \dots) \quad (9)$$

with ξ representing a set of internal state variables.

2.2.2. Direct variational formulation

The equilibrium deformation field is obtained by minimising \mathcal{W} over all deformation fields fulfilling Eq. (8) for an externally prescribed average deformation. Static equilibrium expressed in real and FOURIER² space follows as:

$$\min_{\chi} \mathcal{W} \Rightarrow \text{Div} \mathbf{P}(\mathbf{x}) = \mathcal{F}^{-1}[\mathbf{P}(\mathbf{k})i \mathbf{k}] = \mathbf{0}, \quad (10)$$

which is equivalent to finding the root of the residual body force field

$$\mathcal{F}[\chi(\mathbf{k})] := \mathbf{P}(\mathbf{k})i \mathbf{k} = \mathbf{0}. \quad (11)$$

The differential Eq. (11) in FOURIER space is numerically difficult to solve as it is ill-conditioned. A linear homogeneous reference material with stiffness $\bar{\mathbb{D}}$ (*i.e.*, $\mathbf{P}(\mathbf{x}) = \bar{\mathbb{D}}\mathbf{F}(\mathbf{x})$) allows to reformulate it to an equivalent problem with better numerical properties (Mura, 1987). For a given deformation map χ , equilibrium in this reference material is fulfilled if the residual body force field vanishes

$$\mathcal{P}[\chi(\mathbf{k})] := \bar{\mathbb{D}}[\chi(\mathbf{k}) \otimes i \mathbf{k}]i \mathbf{k} = \mathbf{A}(\mathbf{k})\chi(\mathbf{k}) = \mathbf{0}. \quad (12)$$

The acoustic tensor $\mathbf{A}(\mathbf{k})$ is defined as $\mathbf{A}(\mathbf{k})\mathbf{a}(\mathbf{k}) = \bar{\mathbb{D}}[\mathbf{a}(\mathbf{k}) \otimes i \mathbf{k}]i \mathbf{k}$ for any vector field $\mathbf{a}(\mathbf{k})$. It corresponds to an operator on a deformation map producing the body forces resulting in the reference material. This deformation map vanishes if and only if the body force field vanishes, *i.e.*, in static equilibrium, since $\mathbf{A}(\mathbf{k})$ is non-zero for positive-definite stiffness $\bar{\mathbb{D}}$ and for $\forall \mathbf{k} \neq \mathbf{0}$. Next, an operator which results in the deformation map causing the same body force field in the reference material as a given deformation map in the original material is defined. This corresponds to a preconditioning operation of \mathcal{P}^{-1} on the non-linear operator \mathcal{F} . \mathcal{P} is straightforward to invert since it is local in \mathbf{k} , with $\mathcal{P}^{-1} = \mathbf{A}(\mathbf{k})^{-1}$. The preconditioned system thus reads as

$$\mathcal{P}^{-1}\mathcal{F}[\chi(\mathbf{k})] = \mathbf{A}(\mathbf{k})^{-1}\mathbf{P}(\mathbf{k})i \mathbf{k} = \mathbf{0}, \quad \forall \mathbf{k} \neq \mathbf{0} \quad (13)$$

The deformation gradient field corresponding to this deformation map is obtained from the gradient in real space of Eq. (13)

² Quantities in real space and FOURIER space are distinguished by notation $Q(\mathbf{x})$ and $Q(\mathbf{k})$, respectively, with \mathbf{x} the position in real space, \mathbf{k} the frequency vector in FOURIER space, and $i^2 = -1$. $\mathcal{F}^{-1}[\cdot]$ denotes inverse Fourier transformation.

$$\mathcal{P}^{-1} \mathcal{F}[\chi(\mathbf{k})] \otimes i \mathbf{k} = [\mathbf{A}(\mathbf{k})^{-1} \mathbf{P}(\mathbf{k}) i \mathbf{k}] \otimes i \mathbf{k} = \mathbf{0}, \quad \forall \mathbf{k} \neq \mathbf{0} \quad (14)$$

This is equivalent to Eq. (13) except for a constant residual field, *i.e.*, at $\mathbf{k} = \mathbf{0}$ where the prescribed average deformation gradient is known to hold anyway. Expressed in terms of the deformation gradient field, Eq. (14) can be expressed in FOURIER space as

$$\mathcal{F}_{\text{direct}}[\mathbf{F}(\mathbf{k})] := \mathbf{\Gamma}(\mathbf{k}) \mathbf{P}(\mathbf{k}) = \mathbf{0}, \quad \forall \mathbf{k} \neq \mathbf{0} \quad (15)$$

where the Gamma operator $\mathbf{\Gamma}$ is defined such that $\mathbf{\Gamma}(\mathbf{k}) \mathbf{T}(\mathbf{k}) = [\mathbf{A}(\mathbf{k})^{-1} \mathbf{T}(\mathbf{k}) i \mathbf{k}] \otimes i \mathbf{k}$ for a tensor field $\mathbf{T}(\mathbf{k})$ (Mura, 1987).

2.2.3. Numerical solution

A collocation-based approach at the regular grid points (FOURIER points) in real space is used to discretize Eq. (15), referred to as basic scheme, which results in the system of equations

$$\mathcal{F}_{\text{basic}}[\mathbf{F}(\mathbf{x})] := \mathcal{F}^{-1} \left[\begin{cases} \mathbf{\Gamma}(\mathbf{k}) \mathbf{P}(\mathbf{k}) & \text{if } \mathbf{k} \neq \mathbf{0} \\ \Delta \mathbf{F}_{\text{BC}} & \text{if } \mathbf{k} = \mathbf{0} \end{cases} \right]. \quad (16)$$

The desired deformation BCs \mathbf{F}_{BC} of the volume element are conveniently prescribed by setting $\Delta \mathbf{F}_{\text{BC}} = \bar{\mathbf{F}} - \mathbf{F}_{\text{BC}}$. Adjusting \mathbf{F}_{BC} as outlined by Eisenlohr et al. (2013) allows additionally to prescribe stress BCs component-wise.

The PETSc library (Balay et al., 2013) of non-linear solution methods is utilized to solve the resulting Eq. (16). The residual at an iteration is assembled by evaluating Eq. (16) at the FOURIER points, where the convolution operation is performed in the discrete FOURIER space associated with the grid used by the FFT. Shanthraj et al. (2015) compared three solution methods implemented in PETSc: the non-linear RICHARDSON method, the non-linear generalised minimum residual (non-linear GMRES) method, and the inexact NEWTON-GMRES method. In these methods, an existing solution $\{\square\}_N$ (with $\{\square\}_N =: \{\mathbf{F}(\mathbf{x})\}_N$ in the following) at iteration N is improved until the prescribed convergence criteria are fulfilled. Since the non-linear GMRES shows the best performance, it is used here. In this method, an updated solution, $\{\square\}_{N+1}$, is found as the linear combination of the M previous solutions spanning a KRYLOV subspace $\mathcal{K}_K = \text{span}\{\{\square\}_N, \dots, \{\square\}_{N-M+1}\}$ for which the norm of the linearised residual is minimal

$$\min_{\{\square\}_{N+1} \in \mathcal{K}_K} \left\| \frac{\partial \mathcal{F}}{\partial \{\square\}_N} [\{\square\}_{N+1} - \{\square\}_N] + \mathcal{F} \{\square\}_N \right\|_2 \quad (17)$$

When applied to Eq. (15), compatibility of the deformation gradient field follows from the condition that the updated deformation gradient field is a linear combination of compatible fields.

3. Phenomenological yield functions

In this work, four yield functions, *i.e.*, Yld91, Yld2000-2D, Yld2004-18p, and Yld2007-27p (Barlat et al., 1991, 2003, 2005; Aretz et al., 2010) are investigated. Yld2000-2D is limited to the plane stress state and the other three yield functions are formulated for any general stress states. Φ and ϕ are used to represent the specific yield function and the corresponding equivalent stress, respectively.

3.1. Yld91 yield function

The Yld91 yield function (Barlat et al., 1991) is written as:

$$\Phi = (3I_2)^{n/2} \left\{ \left| 2 \cos \left(\frac{2\theta + \pi}{6} \right) \right|^n + \left| 2 \cos \left(\frac{2\theta + 3\pi}{6} \right) \right|^n + \left| 2 \cos \left(\frac{2\theta + 5\pi}{6} \right) \right|^n \right\} = 2\sigma_y^n \quad \text{with } \theta = \arccos(I_3/I_2^{3/2}) \quad (18)$$

and the equivalent stress is $\phi = (\Phi/2)^{1/n}$. σ_y is the yield stress, which is assumed as the yield stress of uniaxial tension along the rolling direction (RD). I_2 and I_3 are the second and third invariants of the stress tensor, respectively, which can be expressed for the general (anisotropic) case as:

$$I_2 = \frac{(fF)^2 + (gG)^2 + (hH)^2}{3} + \frac{(aA - cC)^2 + (cC - bB)^2 + (bB - aA)^2}{54} \quad (19)$$

$$I_3 = \frac{(cC - bB)(aA - cC)(bB - aA)}{54} + (fF)(gG)(hH) - \frac{(cC - bB)(fF)^2 + (aA - cC)(gG)^2 + (bB - aA)(hH)^2}{6} \quad (20)$$

where $A = \sigma_{22} - \sigma_{33}$, $B = \sigma_{33} - \sigma_{11}$, $C = \sigma_{11} - \sigma_{22}$, $F = \sigma_{23}$, $G = \sigma_{31}$, and $H = \sigma_{12}$. The Yld91 yield function contains six anisotropy parameters (a, b, c, f, g, h), of which a, b, c, h describe the in-plane properties of the sheet. For $n = 2$, the Yld91 yield function reduces to the Hill, 1948 yield function.

3.2. Yld2000-2D yield function

The Yld2000-2D yield function (Barlat et al., 2003) is defined as:

$$\Phi = |\tilde{S}'_1 - \tilde{S}'_2|^n + |2\tilde{S}''_2 + \tilde{S}''_1|^n + |2\tilde{S}''_1 + \tilde{S}''_2|^n = 2\sigma_y^n \quad (21)$$

and the equivalent stress is $\phi = (\Phi/2)^{1/n}$. \tilde{S}'_i and \tilde{S}''_i ($i = 1, 2$) are the principal values of tensors $\tilde{\mathbf{s}}'$ and $\tilde{\mathbf{s}}''$ respectively, which are defined in matrix form for a plane stress case and orthotropic symmetry as:

$$\tilde{\mathbf{s}}' = \begin{bmatrix} \alpha_1 & 0 & 0 \\ 0 & \alpha_2 & 0 \\ 0 & 0 & \alpha_7 \end{bmatrix} \begin{bmatrix} s_{11} \\ s_{22} \\ s_{12} \end{bmatrix}, \quad \tilde{\mathbf{s}}'' = \frac{1}{3} \begin{bmatrix} 4\alpha_5 - \alpha_3 & 2\alpha_6 - 2\alpha_4 & 0 \\ 2\alpha_3 - 2\alpha_5 & 4\alpha_4 - \alpha_6 & 0 \\ 0 & 0 & 3\alpha_8 \end{bmatrix} \begin{bmatrix} s_{11} \\ s_{22} \\ s_{12} \end{bmatrix} \quad (22)$$

where s_{11} , s_{22} , and s_{12} are the deviatoric stress components. The Yld2000-2D yield function contains eight anisotropy parameters (α_i , $i = 1 \dots 8$), all are related to the in-plane properties of the sheet.

3.3. Yld2004-18p yield function

The definition of the Yld2004-18p yield function (Barlat et al., 2005) read as:

$$\begin{aligned} \Phi &= |\tilde{S}'_1 - \tilde{S}'_1|^n + |\tilde{S}'_1 - \tilde{S}'_2|^n + |\tilde{S}'_1 - \tilde{S}'_3|^n + |\tilde{S}'_2 - \tilde{S}'_1|^n + |\tilde{S}'_2 - \tilde{S}'_2|^n + |\tilde{S}'_2 - \tilde{S}'_3|^n + |\tilde{S}'_3 - \tilde{S}'_1|^n + |\tilde{S}'_3 - \tilde{S}'_2|^n + |\tilde{S}'_3 - \tilde{S}'_3|^n \\ &= 4\sigma_y^n, \end{aligned} \quad (23)$$

with the equivalent stress $\phi = (\Phi/4)^{1/n}$. \tilde{S}'_i and \tilde{S}''_i ($i = 1, 2, 3$) are the principal values of tensors $\tilde{\mathbf{s}}'$ and $\tilde{\mathbf{s}}''$, which are defined by two linear transformations of the deviatoric part of the corotational CAUCHY stress $\hat{\mathbf{s}}$:

$$\tilde{\mathbf{s}}' = \mathbf{C} : \hat{\mathbf{s}}; \quad \tilde{\mathbf{s}}'' = \mathbf{D} : \hat{\mathbf{s}} \quad (24)$$

The fourth-order tensors \mathbf{C} and \mathbf{D} characterize the anisotropy of the material, each contains nine material parameters. Expressed in VOIGT notation they read:

$$\mathbf{C} = \begin{bmatrix} 0 & -c_{12} & -c_{13} & 0 & 0 & 0 \\ -c_{21} & 0 & -c_{23} & 0 & 0 & 0 \\ -c_{31} & -c_{32} & 0 & 0 & 0 & 0 \\ 0 & 0 & 0 & c_{44} & 0 & 0 \\ 0 & 0 & 0 & 0 & c_{55} & 0 \\ 0 & 0 & 0 & 0 & 0 & c_{66} \end{bmatrix}, \quad \mathbf{D} = \begin{bmatrix} 0 & -d_{12} & -d_{13} & 0 & 0 & 0 \\ -d_{21} & 0 & -d_{23} & 0 & 0 & 0 \\ -d_{31} & -d_{32} & 0 & 0 & 0 & 0 \\ 0 & 0 & 0 & d_{44} & 0 & 0 \\ 0 & 0 & 0 & 0 & d_{55} & 0 \\ 0 & 0 & 0 & 0 & 0 & d_{66} \end{bmatrix} \quad (25)$$

The Yld2004-18p contains 18 anisotropy parameters, of which c_{55} , c_{66} , d_{55} , and d_{66} describe the out-of-plane properties and the other 14 parameters in the matrices \mathbf{C} and \mathbf{D} in Eq. (25) describe the in-plane properties of the sheet. It has been proven to be an accurate and flexible yield function capable of predicting six or eight “ears” in deep drawing of aluminum sheets (Yoon et al., 2006a,b). Note that when $\mathbf{C} = \mathbf{D}$, i.e., the function accounts for only one transformation, the function reduces to the Yld91 yield function (Barlat et al., 2005).

3.4. Yld2004-27p yield function

The definition of the Yld2004-27p yield function (Aretz et al., 2010) reads as:

$$\begin{aligned} \phi = & \left| \tilde{S}'_1 - \tilde{S}''_1 \right|^n + \left| \tilde{S}'_1 - \tilde{S}''_2 \right|^n + \left| \tilde{S}'_1 - \tilde{S}''_3 \right|^n + \left| \tilde{S}'_2 - \tilde{S}''_1 \right|^n + \left| \tilde{S}'_2 - \tilde{S}''_2 \right|^n + \left| \tilde{S}'_2 - \tilde{S}''_3 \right|^n + \left| \tilde{S}'_3 - \tilde{S}''_1 \right|^n + \left| \tilde{S}'_3 - \tilde{S}''_2 \right|^n + \left| \tilde{S}'_3 - \tilde{S}''_3 \right|^n \\ & + \left| \tilde{S}''_1 - \tilde{S}''_2 \right|^n + \left| \tilde{S}''_2 - \tilde{S}''_3 \right|^n + \left| \tilde{S}''_3 - \tilde{S}''_1 \right|^n = 6\sigma_y^n, \end{aligned} \tag{26}$$

with the equivalent stress $\phi = (\phi/6)^{1/n}$. $\tilde{S}'_i, \tilde{S}''_i$, and \tilde{S}'''_i ($i = 1,2,3$) are the principal values of the tensors $\tilde{\mathbf{s}}', \tilde{\mathbf{s}}''$, and $\tilde{\mathbf{s}}'''$. $\tilde{\mathbf{s}}'$ and $\tilde{\mathbf{s}}''$ are defined the same as that of Yld2004-18p yield function, and $\tilde{\mathbf{s}}''' = \mathbf{E} : \tilde{\mathbf{s}}$. Analogous to \mathbf{C} and \mathbf{D} , the fourth-order tensor \mathbf{E} contains nine material parameters.

4. Architecture of the virtual laboratory

Fig. 1 shows a schematic presentation of the present virtual laboratory based on DAMASK (Roters et al., 2012). DAMASK is a flexible and hierarchically structured approach for modeling a material point behavior and solving of elastoplastic BVPs along with further multiphysics effects. It contains two BVPs solvers, i.e., a spectral method in conjunction with FFT and an in-house developed FEM solver. Also, it provides interfaces to general commercial FEM solvers, e.g., MSC.Marc, ABAQUS/Standard, and ABAQUS/Explicit. The constitutive models implemented into DAMASK range from the phenomenological material model introduced in Section 2.1 to more advanced physically based material models (Ma and Roters, 2004; Roters et al., 2010; Alankar et al., 2011; Cereceda et al., 2016). The various constitutive models render DAMASK a very versatile constitutive and multiphysics modeling approach enabling to simulate materials with different crystal structures (e.g., fcc, bcc, and hcp), different deformation mechanisms (e.g., phase transformation and twinning) and different deformation and microstructure histories.

The virtual laboratory is conveniently implemented as a part of DAMASK in form of an automated script. This script launches virtual tests with automatically generated load cases for the considered RVEs, post-processes the results and finally performs the parameter identification for all selected yield functions until the desired fitting quality is achieved.

The fast and efficient spectral method allows to perform multiple simulations in an affordable time, e.g., the computation time using one Intel Xeon E5-2687W core for an uniaxial tensile simulation (grid size = $120 \times 60 \times 60$, maximum true strain = 0.113) is 450min. This capability is exploited by loading the RVE (see Section 5 for the example used in this study) in many deformation modes which are generated automatically based on a random number generator. After each simulation, in

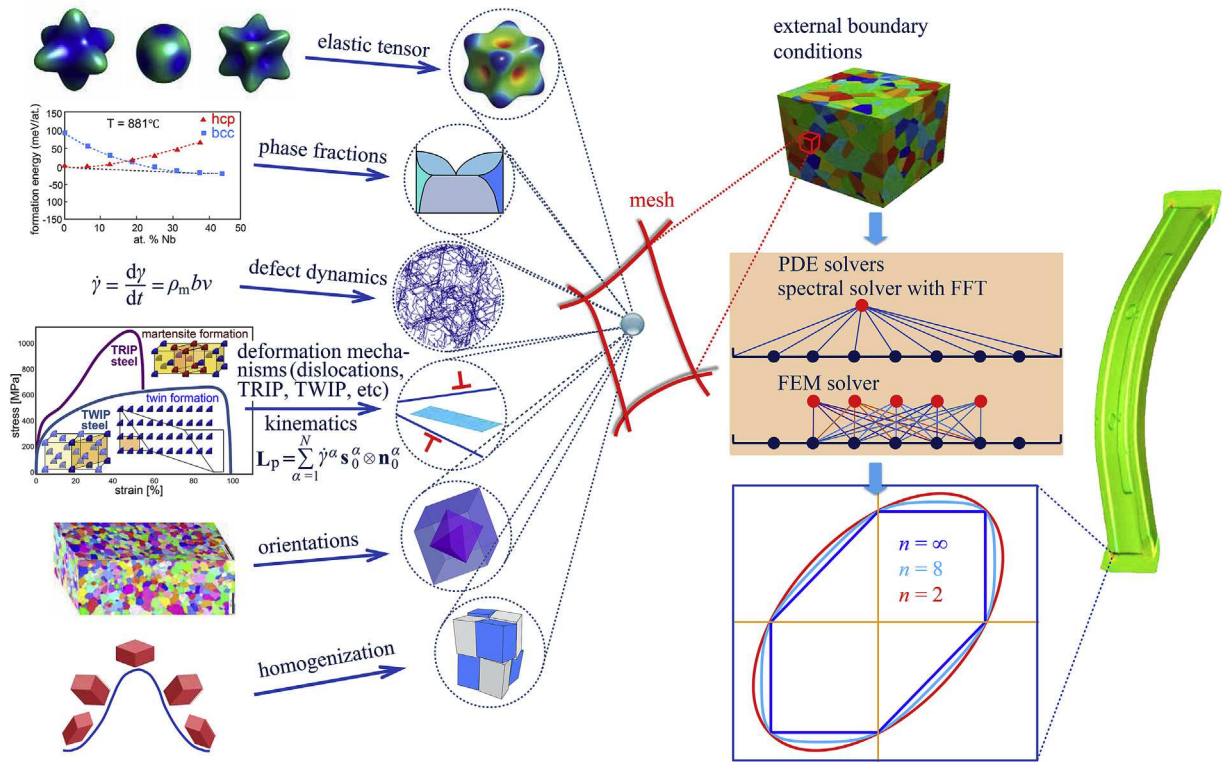


Fig. 1. Yield surface fitting by DAMASK, a multiscale and multiphysics CP modeling framework. The figure shows the various conceptual ingredients with different deformation mechanisms, phases, orientations and homogenization schemes that can be assigned to the same integration/FOURIER point.

a post processing step, the stress tensor for each loading case at the desired level of plastic work per unit volume is determined and used as a yield stress point. Fitting to the yield functions is possible only, if the number of simulations is equal to or larger than the number of parameters of the yield functions. The required fitting procedure can be generally realized by using a nonlinear least square method (NLSM). Here, the LEVENBERG-MARQUARDT NLSM optimization algorithm (Levenberg, 1944; Marquardt, 1963) is employed to find the optimal fitting parameter set and is briefly presented in the following.

Let σ^I ($I = 1, 2, \dots, N$) be a set of stress tensors corresponding to the virtual experimental results (i.e., the yield stress points at the same plastic work per unit volume), $\phi^I = \phi(\sigma^I, \beta)$ be the equivalent stress of the specific yield function, and $\beta = \beta_1, \beta_2, \dots, \beta_M$ be the set of corresponding parameters needed to be identified. The next step then consists in identifying the optimal set of parameters β which minimizes the objective function $O(\beta)$ defined as

$$O(\beta) = \sum_{I=1}^N \left(\frac{\phi(\sigma^I, \beta)}{\sigma_y} - 1 \right)^2 \tag{27}$$

Eq. (27) indicates that all stress points get the same weight assigned in this study. However, generally assigning different weights to rely stronger on certain stress states is possible as well. It should be pointed out that the selection of the data points used in the parameter identification depends substantially on the technical feasibility of performing relevant mechanical tests. For example, many possible combinations exist, r -values, normalized yield stresses, and virtual test data with different weights that could potentially yield adequate fitting fidelity (Grytten et al., 2008; Rabahallah et al., 2009; Aretz and Barlat, 2013; Zhang et al., 2015a; Gawad et al., 2015). Since the virtual laboratory approach provides a large number of yield stress points for any kind of stress or strain modes, in this work, only the yield stress points obtained from the full-field virtual tests were used to identify the required parameters for the considered yield functions. Nevertheless, the prediction of the directionality of the planar anisotropy properties is compared with the data of mechanical tests and virtual tests.

To accelerate and stabilize the solving of the objective function of Eq. (27), the analytical form of the Jacobian matrix is recommended, which is written as:

$$J_{IJ} = \frac{1}{\sigma_y} \frac{\partial \phi(\sigma^I, \beta)}{\partial \beta_J} \quad \text{with } 1 \leq I \leq N \text{ and } 1 \leq J \leq M \tag{28}$$

For fitting more complex yield functions, e.g., Yld2004-18p, the chain rule needs to be employed to calculate the derivative of Eq. (28).

The quality of the determined parameter set $\hat{\beta}$ for β is measure as the root mean square deviation (RMSD) of the residual:

$$\text{RMSD} = \sqrt{\frac{1}{N} \sum_{n=1}^N \left(\frac{\phi(\sigma^I, \hat{\beta})}{\sigma_y} - 1 \right)^2}. \tag{29}$$

For an converging RMSD value, i.e., if additional stress points do not significantly further affect the RMSD value the identification process is stopped. Otherwise, a new simulation is launched until either a predefined maximum number N_{\max} of stress points is reached or the RMSD value is converged. To reduce computation time, a predefined number of simulations can be run in parallel.

Additionally, virtual uniaxial tensile experiments were performed in different directions from the RD to the transverse direction (TD). As illustrated in Fig. 2(a), θ denotes the uniaxial tensile direction, which is measured between the longitudinal

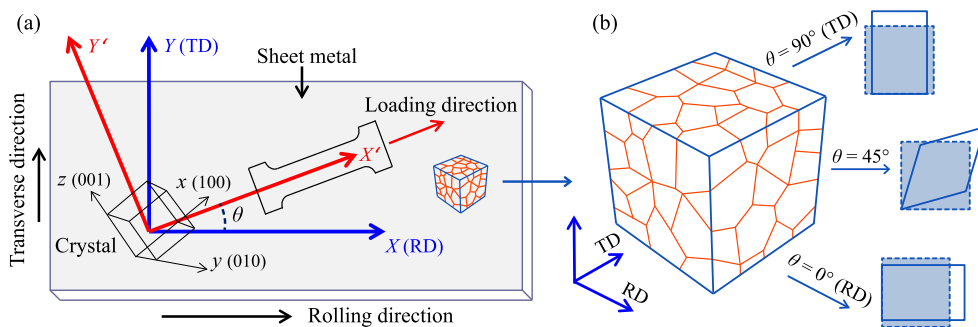


Fig. 2. (a) Illustration of the reference frame set-up for conducting simulated tensile tests in arbitrary loading directions and the corresponding texture rotation in the virtual uniaxial tensile experiments, and (b) the deformed shapes of the corresponding RVE under the uniaxial tensile simulations with different loading directions, i.e., $\theta = 0^\circ$ (RD), $\theta = 45^\circ$, and $\theta = 90^\circ$ (TD).

axis of the specimen and the RD. In DAMASK, it is convenient to apply periodic BCs on the RVE for uniaxial tensions in different directions. However, if the loading direction is not placed along the RD ($\theta = 0^\circ$) or the TD ($\theta = 90^\circ$), the deformed shape of the RVE in the RD-TD plane will not assume a rectangular shape, e.g., a diamond shape will be obtained for the case of $\theta = 45^\circ$, as shown in Fig. 2(b). Such non-rectangular shapes make it inconvenient to calculate the r -values. We therefore use an equivalent approach to perform uniaxial tensile tests. For example, if the uniaxial tensile direction is aligned along the angle θ , we simply rotate the sample coordinate system $[XYZ]$ ([RD-TD-ND], with ND denoting normal direction) to a new system $[X'Y'Z']$ where X' and Z' coincide with the loading direction and the ND, respectively. Then the orientation of the grains in the new reference system becomes $\{\varphi_1 - \theta, \Phi, \varphi_2\}$ as outlined in Appendix A. As a result, the loading directions of all the virtual uniaxial tensile experiments are the same as those of the uniaxial tension tests conducted along the RD.

The subsequent rotation intervals of θ from the RD towards the TD are 7.5° , i.e., 13 virtual uniaxial tensile tests were conducted for each case. The advantage of such transformation is that the deformed shapes of RVE always follow the uniaxial tension, which is favorable for calculating r -values.

5. Model generation from experimental microstructures

5.1. Material characterization

The anisotropy of the commercial AA3104 aluminum alloy in sheet metal forming is investigated as a model system in this study. This material is especially designed for beverage can production and is processed in a way to finally produce small “ears” in the cup-drawing operation (Raabe et al., 2003; Engler et al., 2011). Two different material states, corresponding to two different textures are used: (i) The hot-band (as-received) sample is the annealed AA3104 aluminum alloy after hot rolling, i.e., in the fully recrystallized state. (ii) The cold-rolled sample is produced from this state by rolling it under near-plane strain conditions until the thickness is reduced to 50%. The crystallographic textures of both samples were measured by an FEI Nova 400 field emission scanning electron microscope (FE-SEM) equipped with an electron backscatter diffraction (EBSD) system. The size of the EBSD mapping area is $0.6 \text{ mm} \times 0.6 \text{ mm}$ with a step size of $2 \mu\text{m}$ for the hot-band sample, and $0.12 \text{ mm} \times 0.12 \text{ mm}$ with a step size of $0.4 \mu\text{m}$ for the cold-rolled sample. Owing to the orthotropic symmetry of the rolled sheet and the cubic crystal symmetry (Bunge, 1982), $\varphi_1, \Phi, \varphi_2$ vary in the reduced EULER space between 0° and 90° . The EBSD maps and orientation distribution functions (ODFs) of the hot-rolled and cold-rolled samples are shown in Figs. 3, 4(a), and 5(a).

The micro-texture mapped by SEM-EBSD contains in the present case a large number of grains and orientations, hence sufficient statistics is given. The hybrid integer approximation method introduced by Eisenlohr and Roters (2008) is adopted to reconstruct the ODFs derived from these EBSD data sets using a limited set of discrete orientations from the experimentally obtained ODFs. Figs. 4(b) and 5(b) show the reconstructed ODFs using 500 discrete orientations for both material states. The root mean squared deviations (RMSD) (Eisenlohr and Roters, 2008) between the reconstructed ODFs and the experimental ODFs are 4.482% and 4.458% for the hot-band case and the cold-rolled case, respectively, which indicate a good reproduction fidelity of the reconstructed ODFs.

Fig. 4 shows that the texture of the hot-band sample mainly consists of a strong Cube component and a weak Goss component. Fig. 5 shows that the texture of the cold-rolled sample contains a strong S components, a moderate Brass component and a weak Copper components. The strong Cube component of the hot-band sample has almost disappeared. It

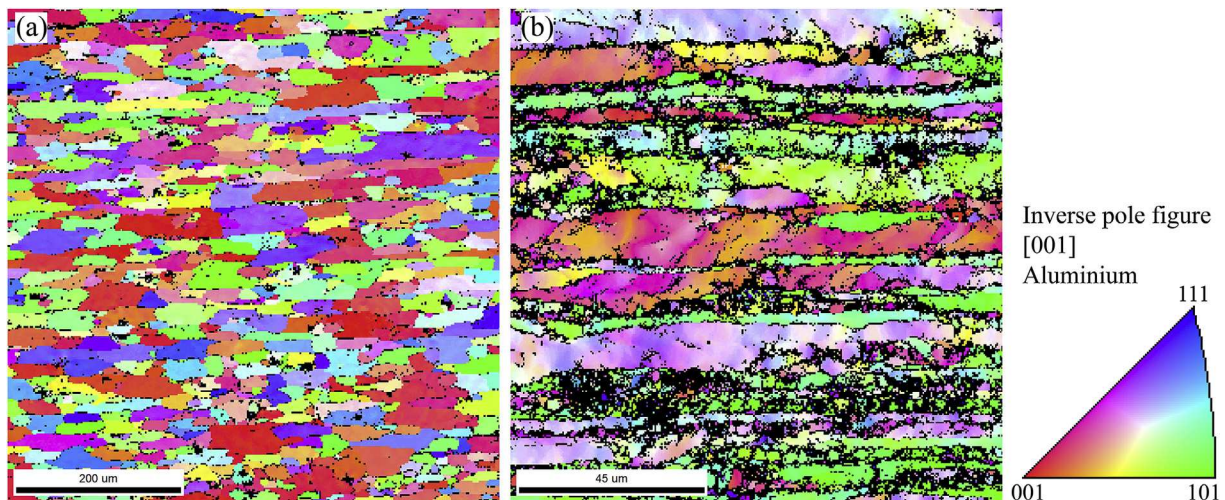


Fig. 3. EBSD maps of AA3104 aluminum alloy sheets, (a) as-received after hot rolling; (b) cold-rolled to 50% thickness reduction.

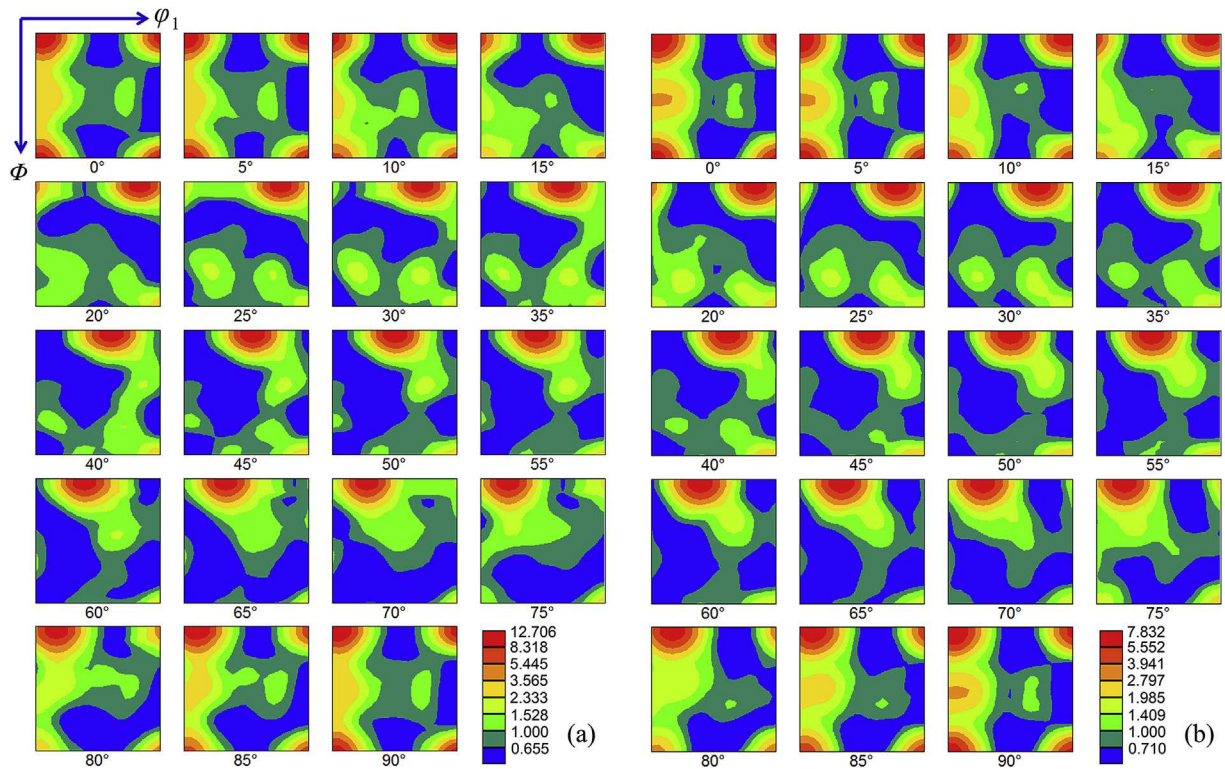


Fig. 4. Orientation density maps obtained from the ODFs as sections through the reduced EULER space for cubic-orthorhombic symmetry of the hot-band AA3104 aluminum alloy sheet (constant φ_2 sections, 0° to 90° in 5° steps, EULER angles in BUNGE's convention), (a) experiment; (b) reconstructed using 500 discrete orientations.

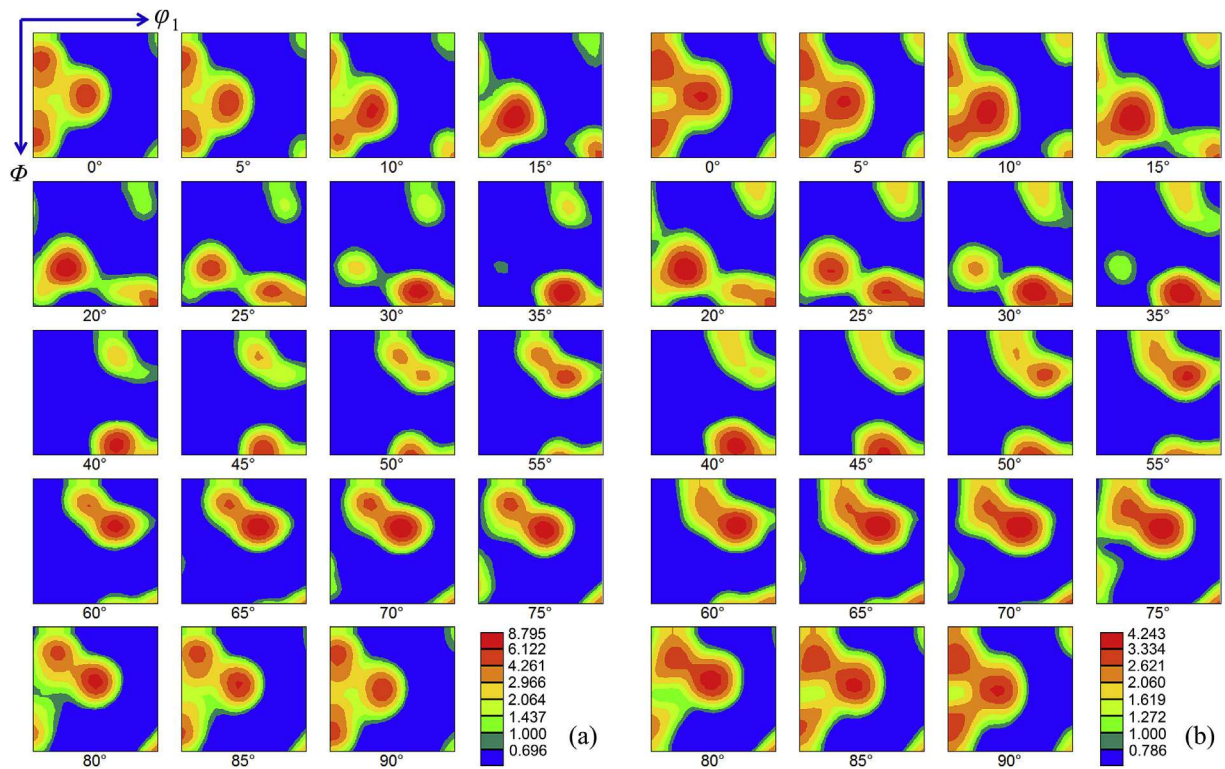


Fig. 5. Orientation density maps obtained from the ODFs as sections through the reduced EULER space for cubic-orthorhombic symmetry of an AA3104 aluminum alloy sheet after cold-rolling to 50% thickness reduction (constant φ_2 sections, 0° to 90° in 5° steps, EULER angles in BUNGE's convention), (a) experiment; (b) reconstructed using 500 discrete orientations.

should be noted that the reconstructed ODFs are less sharp than the experimentally obtained ODFs, *i.e.*, some quantitative differences can be observed: The Cube component is weakened while the Goss component is strengthened for the hot-band sample, the S component is weakened while the Brass and Copper components are slightly strengthened for the case of the cold-rolled sample. The textures shown in Figs. 4(b) and 5(b) are used as texture input data for the subsequent virtual laboratory simulations.

5.2. Material constants

The constitutive parameters used in the current CP model are adjusted to experimental data of Wu et al. (2003), *i.e.*, to a cold-rolled AA3104 aluminum alloy. The used material constants are listed in Table 1, and the computed stress–strain curve is given together with the experimental one in Fig. 6. The same set of material constants given in Table 1 is used for both, the hot-band and the cold-rolled sample in this work. Even though the cold-rolled sample is harder than the hot-band sample, this does not introduce a bias to the results as only normalized yield stress values are of interest. Moreover, only the initial yielding is investigated and all slip systems in the fcc lattice belong to the $\{110\}\langle 111 \rangle$ family and, hence, show the same strain hardening characteristics. Therefore, the influence of the difference in flow stress between the two material states on the anisotropy should be negligible compared to that of the crystallographic textures.

5.3. Representative volume elements

As stated above, the virtual laboratory was applied to generate random yield stress points for the identification of various yield functions and to perform the virtual uniaxial tensile tests to obtain the planar anisotropic properties, *i.e.*, the r -values and the normalized yield stresses. For the former one, *i.e.*, to generate random yield stress points, a cubic RVE, labelled as RVE1 (Fig. 7(a)), was used for the virtual tests of both, the hot-band and the cold-rolled samples. It was discretized by $64 \times 64 \times 64$ FOURIER points, and applied a large number of periodic BCs corresponding to arbitrary deformation modes. For the uniaxial tensile test simulations, RVE2 (Fig. 7(b)) with equiaxed crystal structures was adopted for the hot-band case. As the tensile deformation in the x axis is significantly larger than the compressive deformations in the y and z axes, RVE2 was discretized by $120 \times 60 \times 60$ FOURIER points.

Although the crystallographic texture plays a predominant role in affecting the mechanical anisotropy, the average grain shape could also contribute to a modification of the directional response of rolled materials (Haouaoui et al., 2006; Delannay and Barnett, 2012). For example, Choi et al. (2000) applied the VPSC model to investigate the influence of grain morphology on macroscopic anisotropy of cold-rolled AA5019 sheet. The authors found that simulations with the ellipsoidal grain shape show better reproduction of experimental data than those with spherical grain shape when predicting the deformation anisotropy. Delannay et al. (2009) investigated the planar anisotropy of two cold-rolled steel sheets by using CPFEM, VPSC, and LAMEL model formulations, and found that the grain shape effect is less important than the texture effect, but it is not

Table 1

Material parameters of AA3104 aluminum alloy according to the experimental data of Wu et al. (1998, 2003), the unit of, C_{11} , C_{12} and C_{44} is GPa, g_0 , g_∞ and h_0 is MPa, and $\dot{\gamma}_0$ is s^{-1} .

C_{11}	C_{12}	C_{44}	g_0	g_∞	h_0	$\dot{\gamma}_0$	m	a
206	118	54	88	118	2483	10^{-3}	0.02	2

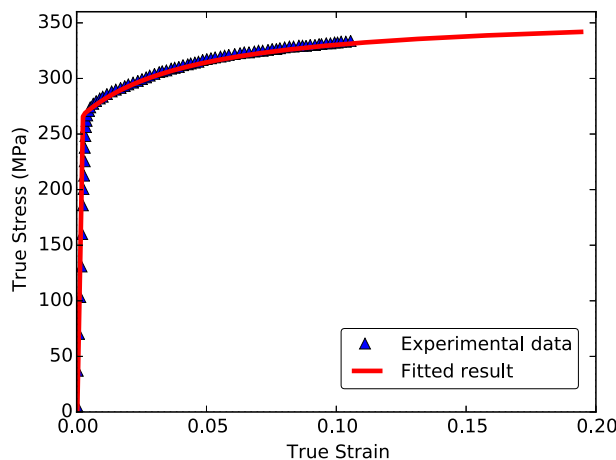


Fig. 6. Experimentally obtained and simulated stress–strain curves of the cold-rolled AA3104 aluminum alloy. Experimental data is taken from Wu et al. (2003).

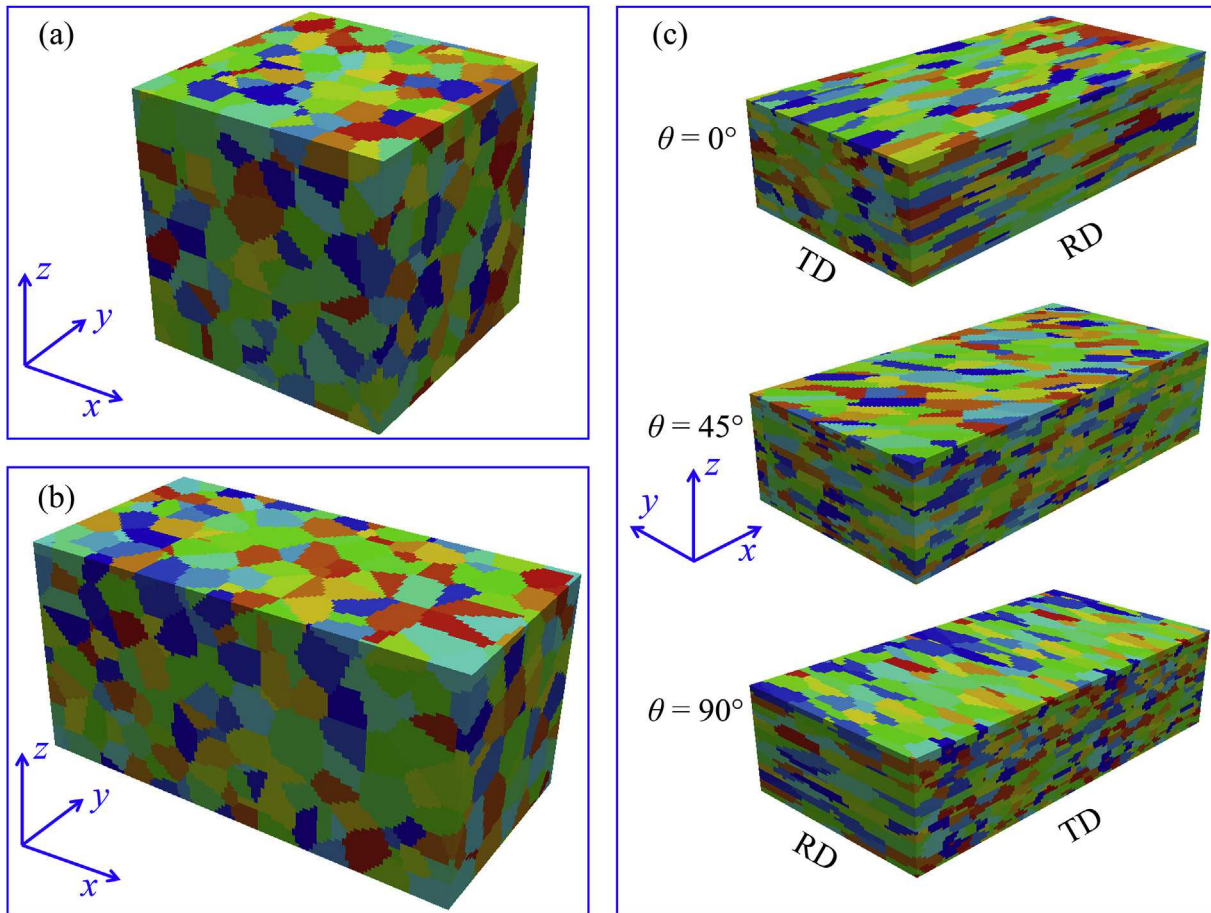


Fig. 7. RVEs with 500 randomly distributed grains, (a) RVE1 used for the parameter identification, size = 64^3 ; (b) RVE2 used for the virtual uniaxial tensile tests, size = $120 \times 60 \times 60$; (c) examples of RVE3 with the directional cold-rolled grain morphologies used for the uniaxial tensile tests, size = $160 \times 80 \times 40$. x is the loading direction, z is the (sheet) normal direction.

negligible. Consequently, thirteen RVEs (referred to RVE3) with the directional cold-rolled grain morphologies were used for the uniaxial tensile tests and plane strain tensile tests of the cold-rolled sample, as exemplified in Fig. 7(c). RVE3 was discretized by using $160 \times 80 \times 40$ FOURIER points.

All the RVEs in Fig. 7 contain 500 randomly distributed grains, and the representative polycrystalline aggregates were generated by a standard VORONOI tessellation. Therefore, RVE1, RVE2, and RVE3 have about 524, 864 and 1024 FOURIER points per grain, respectively, and hence represent the microstructure of the considered material with a high resolution as shown in Fig. 7. The 500 discrete orientations shown in Fig. 4(b) (for the hot-band case) and Fig. 5(b) (for the cold-rolled case) were assigned randomly to the polycrystalline aggregates.

6. Results and discussion

In total, 125 randomly generated load cases were used for RVE1 with hot-band and cold-rolled textures to fit the yield surface functions. The yield stresses at a plastic work per unit volume of 1 MPa were used to identify the parameters of the considered yield functions. The identified parameters are documented in Tables 2–4, where “2D” indicates that all stress points belong to a plane stress state, while “3D” denotes an arbitrary general stress state, *i.e.*, including stress components along thickness direction. Besides the parameters of the respective yield functions, the exponent n is also an undetermined parameter in this work. Tables 2–4 show that, the exponents n of the Yld91 and Yld2000-2D yield functions are determined as less than six, while the exponents n of the Yld2004-18p and Yld2004-27 yield function are determined to lay in a range between 6.46 and 7.34. This is different from the recommendations of Hosford (1972), who suggested a value of $n = 8$ for isotropic fcc materials and $n = 6$ only for bcc metals. However, it should be noted that these recommendations are based on the yield surfaces calculated by the TBH model (which gives, as outlined in Section 1, the upper bound) for randomly oriented polycrystals and other values of n may apply for materials with a strong initial texture. In this work, $n = 6$ seems preferable for

Table 2

Parameters identified for fitting the Yld91 yield function (Barlat et al., 1991) determined for the hot-band and cold-rolled AA3104 aluminum alloy.

	<i>a</i>	<i>b</i>	<i>c</i>	<i>f</i>	<i>g</i>	<i>h</i>	<i>n</i>
Hot-band 2D	1.0061	1.0736	0.9989	–	–	0.9539	5.7917
Hot-band 3D	0.9976	1.0615	1.0315	0.9759	0.9525	0.9627	5.3041
Cold-rolled 2D	0.9933	1.0822	0.9567	–	–	0.9940	5.5410
Cold-rolled 3D	0.9632	1.0904	1.0058	–1.0407	0.9652	0.9984	5.2524

Table 3

Parameters identified for fitting the Yld2000-2D (Barlat et al., 2003) yield function determined for the hot-band and cold-rolled AA3104 aluminum alloy.

	<i>a</i> ₁	<i>a</i> ₂	<i>a</i> ₇	<i>a</i> ₃	<i>a</i> ₄	<i>a</i> ₅	<i>a</i> ₆	<i>a</i> ₈	<i>n</i>
Hot-band	0.9349	1.0671	0.9097	0.9690	0.9861	1.0452	0.9999	1.0805	5.9992
Cold-rolled	0.8734	1.0760	0.9594	0.9820	0.9597	1.0600	1.0294	1.0490	5.9630

Table 4

Parameters identified for fitting the Yld2004-18p and Yld2004-27p yield functions (Barlat et al., 2005; Aretz et al., 2010) determined for the hot-band and cold-rolled AA3104 aluminum alloy.

	Yld2004-18p				Yld2004-27p			
	Hot-band		Cold-rolled		Hot-band		Cold-rolled	
	2D	3D	2D	3D	2D	3D	2D	3D
<i>c</i> ₁₂	0.8841	1.1533	1.0799	1.6544	1.1237	0.6983	1.1966	0.4116
<i>c</i> ₂₁	1.1456	1.6206	1.0552	1.0574	0.9623	1.9106	0.7589	–0.1486
<i>c</i> ₂₃	1.1845	0.9688	0.7840	0.3627	0.4378	1.0230	0.8237	0.9442
<i>c</i> ₃₂	0.7411	0.6850	0.7378	0.9463	0.9356	1.3343	0.8413	0.8021
<i>c</i> ₃₁	0.9972	0.9189	0.6443	0.6858	1.0118	1.0041	1.1270	0.0023
<i>c</i> ₁₃	1.1305	1.4709	0.8626	1.5519	0.8256	–0.0410	0.7199	–0.7082
<i>c</i> ₄₄	1.1222	1.4253	1.0518	1.3350	0.6181	–0.7932	0.7872	0.8973
<i>c</i> ₅₅	–	0.7399	–	0.9551	–	0.4726	–	0.5934
<i>c</i> ₆₆	–	1.1367	–	0.9857	–	0.3504	–	0.6497
<i>d</i> ₁₂	0.9294	–0.3329	0.4223	0.0167	0.8762	–0.5786	1.0040	0.0286
<i>d</i> ₂₁	0.9506	1.0360	1.0096	0.4957	1.0380	0.4470	1.0264	–1.6150
<i>d</i> ₂₃	0.6239	1.4072	1.0345	1.0638	1.1692	0.7778	0.9299	–0.5154
<i>d</i> ₃₂	0.9561	0.7698	1.1961	1.2335	1.0969	0.4226	0.8219	0.0761
<i>d</i> ₃₁	1.0975	0.8263	1.3817	0.7865	1.0874	0.0314	0.6162	1.0769
<i>d</i> ₁₃	0.7071	0.4204	1.1467	0.5736	1.2099	0.0313	1.3520	–0.7057
<i>d</i> ₄₄	0.6966	0.2457	0.8549	0.5363	1.1455	0.8730	1.1826	1.0061
<i>d</i> ₅₅	–	1.1198	–	1.0686	–	1.0774	–	1.3723
<i>d</i> ₆₆	–	–0.6515	–	0.8454	–	1.2673	–	0.7815
<i>e</i> ₁₂	–	–	–	–	0.8981	0.9298	–0.0037	1.0561
<i>e</i> ₂₁	–	–	–	–	0.8667	0.8665	0.5699	1.1506
<i>e</i> ₂₃	–	–	–	–	0.9640	0.7021	1.1133	1.0310
<i>e</i> ₃₂	–	–	–	–	0.9936	0.770	0.9759	1.0506
<i>e</i> ₃₁	–	–	–	–	0.9087	1.0442	0.6743	1.1716
<i>e</i> ₁₃	–	–	–	–	0.9339	1.3839	0.5781	0.8645
<i>e</i> ₄₄	–	–	–	–	0.9512	1.0962	0.9267	0.9650
<i>e</i> ₅₅	–	–	–	–	–1.7468	1.0939	–1.9112	0.9859
<i>e</i> ₆₆	–	–	–	–	–1.8016	0.9461	–1.9983	1.0845
<i>n</i>	7.0125	6.6847	7.3438	6.6047	7.2143	6.4637	6.8089	7.0129

an AA3014 aluminum alloy for both, the recrystallized state and the cold-rolled state. The determined parameters of the considered yield functions can be used to derive the in-plane normalized yield stresses, *r*-values, and the yield surfaces in the *xy* plane. All the ensuing results and discussions are based on these identified parameters, and limited to the plane stress state.

Fig. 8 shows the RMSD of the yield functions (see Eq. (29)) versus the number of input stress points *N*. Except for the Yld91 yield function, all other three yield functions show a relatively small (less or about 1.0%) and close RMSD at the end of identification with all curves being converged to a stationary value. This indicates that the fitting capacity of the Yld91 yield function is limited in comparison to the other formulations considered, of which the Yld2004-18p and Yld2004-27p yield functions show the best performance. The observations can be explained by the number of parameters: the Yld2004-27p yield function is the most flexible function, as it has 27 parameters for the 3D case and 21 parameters for the 2D case, while the Yld91 yield function has a lower number of anisotropy parameters, namely, six for the 3D and four for the 2D case. Even for the Yld91 yield function, however, the RMSD value reached at the end of the identification protocol is below 1.8% for the hot-band sample and below 1.6% for the cold-rolled sample. This result reveals that all the identified yield functions show

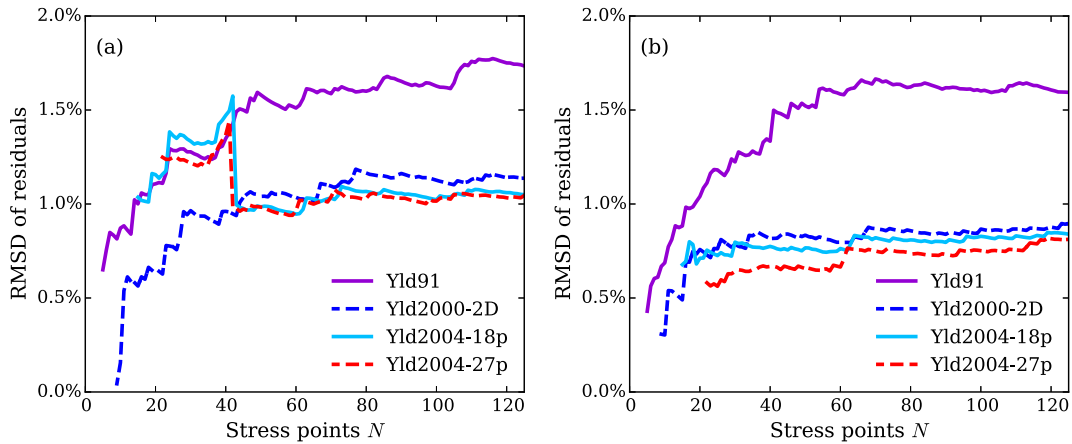


Fig. 8. RMSD of the yield functions versus the number of input yield stress points N , (a) for the hot-band AA3104 aluminum alloy; (b) for the cold-rolled AA3104 aluminum alloy. Yld91, Yld2000-2D (for the plain stress state), and Yld2004-18p are the yield functions proposed by Barlat et al. (1991, 2003, 2005). Yld2004-27p is the yield function proposed by Aretz et al. (2010).

a good capability in representing the computed yield stress points. Furthermore, the Yld2000-2D yield function which requires less parameters compared with the Yld2004-18p and Yld2004-27p yield functions is sufficient to fit the large number of yield stress points of both samples.

6.1. Deformation and strength anisotropy

Figs. 9–13 show a comparison of the deformation anisotropy (r -value) and strength anisotropy (normalized yield stresses, Y_θ) predicted by the considered yield functions with those of the virtual uniaxial tensile tests (see Section 4) and mechanical experiments. The r -value and Y_θ are calculated at a plastic work per unit volume of 1, 2.5, 7.5, and 15 MPa, respectively. The comparison reveals that the influence of plastic deformation on both, deformation anisotropy and strength anisotropy is low, in other words, the change of texture and, hence, anisotropy induced by the deformation is negligible.

Fig. 9 shows the predicted r -values of the hot-band sample versus θ for the identified yield functions in comparison to the r -values obtained from the virtual uniaxial tensile tests. The highest r -value is in the TD while the lowest value is in the direction of $\theta = 45^\circ$. It is found that the results of the yield functions, i.e., Yld2000-2D, Yld2004-18p, and Yld2004-27p match well with that of the virtual tensile tests, while Yld91 overestimates the r -values in most directions. Fig. 10 shows a comparison between the predicted Y_θ of the yield functions with that of the virtual tests. The Y_θ in the TD is higher than that in the

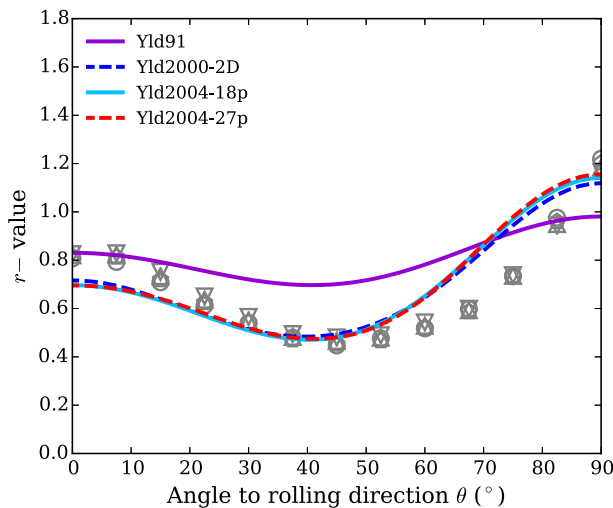


Fig. 9. r -value versus θ of the hot-band AA3104 aluminum alloy. The solid lines are the predictions of the identified yield functions. The open symbols are the results obtained from the virtual laboratory simulations (\circ , \diamond , Δ , ∇ correspond to a plastic work per unit volume of 1, 2.5, 7.5, and 15 MPa, respectively). Yld91, Yld2000-2D (for the plain stress state), and Yld2004-18p are the yield functions proposed by Barlat et al. (1991, 2003, 2005). Yld2004-27p is the yield function proposed by Aretz et al. (2010).

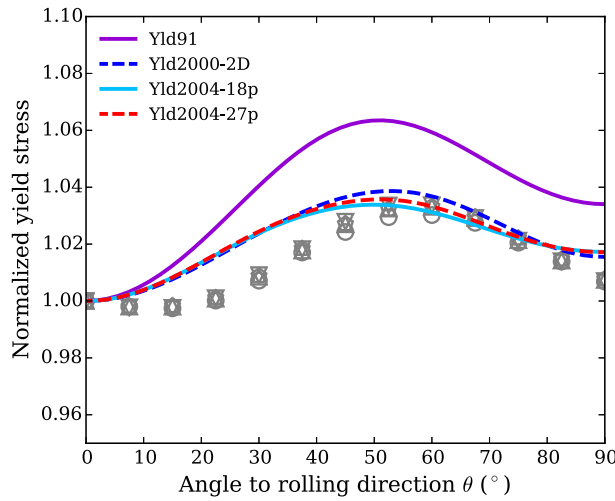


Fig. 10. Normalized yield stress Y_θ versus θ of the hot-band AA3104 aluminum alloy. The solid lines are the predictions of the identified yield functions. The open symbols are the results obtained from the virtual laboratory simulations (\circ , \square , Δ , ∇ correspond to a plastic work per unit volume of 1, 2.5, 7.5, and 15 MPa, respectively). Yld91, Yld2000-2D (for the plain stress state), and Yld2004-18p are the yield functions proposed by Barlat et al. (1991, 2003, 2005). Yld2004-27p is the yield function proposed by Aretz et al. (2010).

RD. The virtual uniaxial tensile results indicate that the deep drawing cup of the hot-band AA3104 aluminum alloy will produce four “ears” near $\theta = 15^\circ, 105^\circ, 195^\circ,$ and 285° . It is found again that the Yld2000-2D, Yld2004-18p, and Yld2004-27p yield functions match the virtual tests results obtained from the full-field simulations better than the Yld91 yield function. According to Barlat et al. (1997), it is not possible for the Yld91 yield function to represent the anisotropy of a strong recrystallization texture dominated by the Cube and Goss texture components. The virtual uniaxial tension tests show that the r -values vary in the range of 0.45–1.2 while the Y_θ varies in the range of 0.997–1.033, *i.e.*, the hot-band AA3104 aluminum alloy shows strong deformation anisotropy but weak strength anisotropy.

No experimental tensile data are considered for the hot-band sample, however, as discussed above, the main texture components of the hot-band case are a strong Cube component and a weak Goss component. The anisotropic properties of materials with the common ideal texture components can be found in the work of Arminjon and Bacroix (1991) and Darrieulat and Piot (1996). Comparing Figs. 9 and 10 with the results from Arminjon and Bacroix (1991) and Darrieulat and Piot (1996), it can be observed that the r -values and Y_θ obtained from the virtual uniaxial tensions are clearly affected by the presence of the Cube and Goss orientations. For the r -values, a valley appears near $\theta = 45^\circ$, and this position is correctly captured by both, the virtual tensile tests and the yield surface predictions. In contrast, the peak of Y_θ shown in Fig. 10 appears

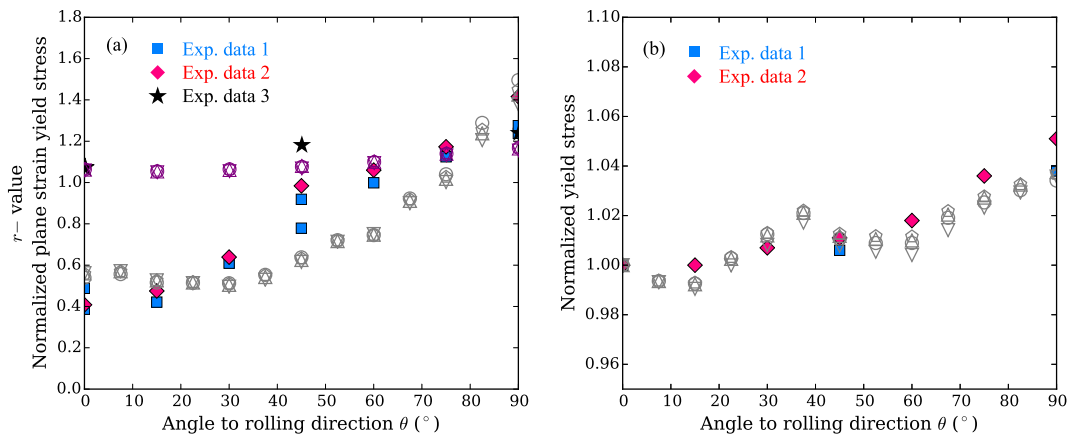


Fig. 11. r -value versus θ (a) and normalized yield stress Y_θ versus θ (b) of the cold-rolled AA3104 aluminum alloy. The open symbols are the results obtained from the virtual laboratory simulations (\circ , \square , Δ , ∇ correspond to a plastic work per unit volume of 1, 2.5, 7.5, and 15 MPa, respectively). The solid symbols are experimental data from Wu et al. (2003) (Exp. data 1), Aretz et al. (2010) (Exp. data 2), and Aretz et al. (2010) (Exp. data 3). The purple open symbols in (a) represent the normalized plane strain yield stress obtained from virtual tests, while data 3 refers to the corresponding experimental results.

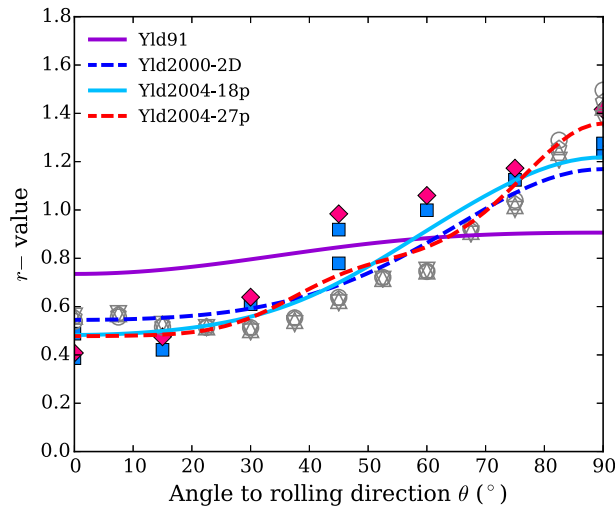


Fig. 12. r -value versus θ of the cold-rolled AA3104 aluminum alloy. The solid lines are the predicted results of the identified yield functions. The meaning of the symbols is the same as that in Fig. 11. Yld91, Yld2000-2D (for the plain stress state), and Yld2004-18p are the yield functions proposed by Barlat et al. (1991, 2003, 2005). Yld2004-27p is the yield function proposed by Aretz et al. (2010).

near $\theta = 52.5^\circ$ for the yield functions and $\theta = 60^\circ$ for the virtual tests. Obviously, these positions result from the combined contributions of the Cube and Goss orientations, and since the Cube orientation is stronger than the Goss orientation, its peak value is smaller than the one produced by the Goss orientation.

For the cold-rolled case, the experimental results of Wu et al. (2003), Aretz and Barlat (2013), and Aretz et al. (2010) are adopted for comparison, as shown in Fig. 11. It can be seen that, in spite of some scatter in the experimental data, the results of the virtual tensile tests obtained by the full-field simulation show good agreement with these experimental results. It indicates that the virtual laboratory presented could be a substitute for the elaborated mechanical tests of plastic anisotropy. The comparison between the plane strain tensile stresses obtained by the virtual laboratory and the mechanical tests from Aretz et al. (2010) is also superposed in Fig. 11(a). The yield stresses of plane-strain tensile tests along the RD and TD match well with the experimental results, while the yield stress of test along the direction with $\theta = 45^\circ$ show some deviation with the corresponding experimental result. Fig. 11 also implies that, the planar anisotropy of the cold-rolled sample is more complex than that of the hot-band sample, and the deep drawing cup of the cold-rolled AA3104 aluminum alloy will produce eight small “ears”.

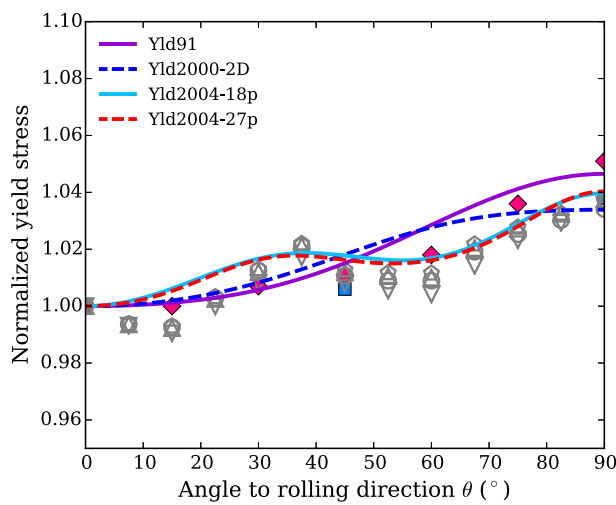


Fig. 13. Normalized yield stress Y_θ versus θ of the cold-rolled AA3104 aluminum alloy. The solid lines are the predicted results of the identified yield functions. The meaning of the symbols is the same as that in Fig. 11. Yld91, Yld2000-2D (for the plain stress state), and Yld2004-18p are the yield functions proposed by Barlat et al. (1991, 2003, 2005). Yld2004-27p is the yield function proposed by Aretz et al. (2010).

Fig. 11 is shown again together with the predicted values of the yield functions in Figs. 12 and 13. Fig. 12 reveals that the predicted r -values increase monotonically with respect to θ , *i.e.*, they are lowest at $\theta = 0^\circ$ and highest at $\theta = 90^\circ$. Except for the Yld91 yield function, all yield functions yield quantitatively correct r -values and capture the shape of r -values versus θ . Moreover, small “waves” can be observed in the curve predicted by the Yld2004-27p yield function, this is because Yld2004-27 is the most flexible one which is able to represent even more complex shapes. Fig. 13 shows that the maximum strength anisotropy of the cold-rolled sample appears in the TD, *i.e.*, about 1.038. Though the strength anisotropy of the cold-rolled sample is slightly larger than that of the hot-band sample, it is still comparably small. It is not surprising as the considered material has been designed to produce very small “ear” in beverage can fabrication (Aretz and Barlat, 2013). As Y_θ varies only in the range of 0.992–1.038, such small fluctuation may render it especially challenging to capture the complex shape of Y_θ versus θ for the case of the cold-rolled sample. However, the identified yield functions Yld2004-18p and Yld2004-27p successfully predict the magnitudes and shape of Y_θ versus θ , while the yield functions Yld91 and Yld2000-2D give a reasonable prediction of the magnitudes.

It must be noted that both, the r -values and the normalized yield stresses obtained from the virtual uniaxial tensile tests and the experiments, are not used in the identification process. All the identified yield functions, however, provide a high-accuracy fitting of yield stress points, and still, the identified yield functions, except for Yld91, show good performance in the prediction of the r -values and the normalized yield stresses. This means that the procedure used here for the parameter identification using the virtual laboratory simulation method is reliable and thus applicable to a wider range of corresponding sheet metal forming problems involving plastic anisotropy.

6.2. Yield surfaces

Figs. 14 and 15 show the comparison between the predicted yield surfaces and the 2D (xy -plane) yield stress points generated by the virtual laboratory at a plastic work per unit volume of 1 MPa, where $\bar{\sigma}$ denotes the uniaxial tensile yield stress along the RD obtained from the virtual tests. For the cold-rolled case, the experimental data of Wu et al. (2003) were also added for comparison. It is seen that all the yield functions are able to fit these stress points well, and the experimental stress points are adequately reproduced by the yield stress points of the virtual tests. For both, the hot-band and the cold-rolled cases, the differences between yield surfaces of the identified four yield functions are relative small, and the yield surfaces of Yld2004-18p and Yld2004-27 are almost completely identical. Only the yield surface obtained by using the Yld91 yield function shows a minor difference to the others being a little more smooth in the region around equibiaxial tension for both cases. This is because the Yld91 yield function is less flexible than the others due to its smaller number of fitting parameters.

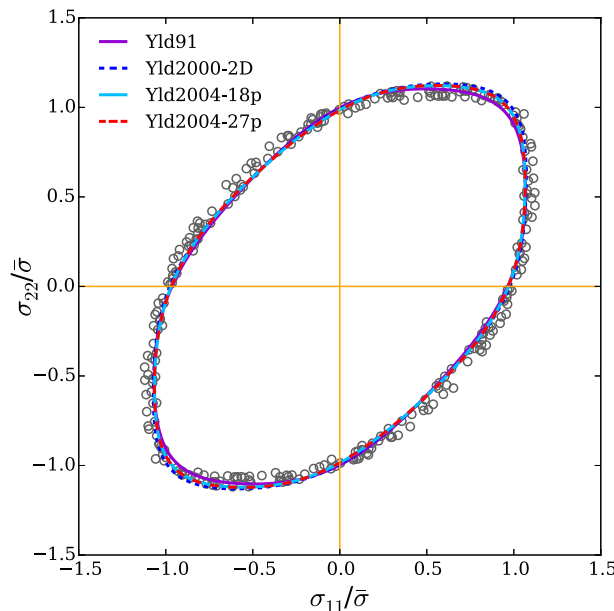


Fig. 14. Yield surfaces ($\sigma_{12} = 0$) of the hot-band AA3104 aluminum alloy predicted by the identified yield functions. $\bar{\sigma}$ denotes the uniaxial tensile yield stress along the RD obtained from the virtual tests. The symbols “○” are the yield stress points provided by the virtual laboratory simulations. Yld91, Yld2000-2D (for the plain stress state), and Yld2004-18p are the yield functions proposed by Barlat et al. (1991, 2003, 2005). Yld2004-27p is the yield function proposed by Aretz et al. (2010). The yield surfaces predicted by the identified Yld2000-2D, Yld2004-18p, and Yld2004-27p yield functions are almost the same, especially, the ones predicted by the Yld2004-18p and Yld2004-27p yield functions overlap each other.

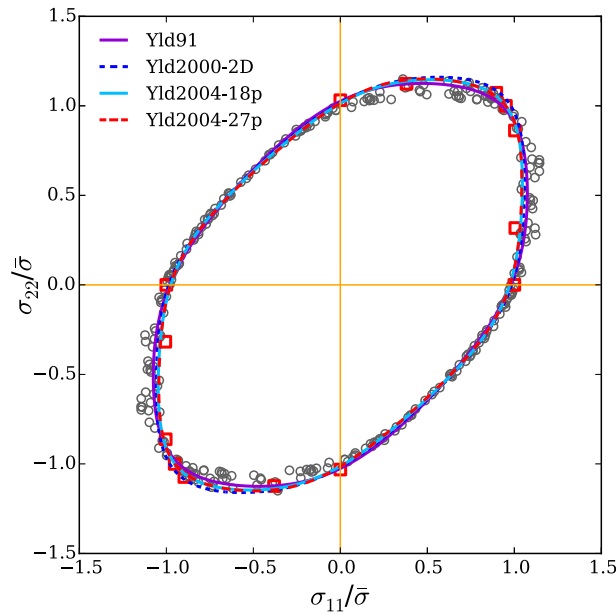


Fig. 15. Yield surfaces ($\sigma_{12} = 0$) of the cold-rolled AA3104 aluminum alloy predicted by the identified yield functions. $\bar{\sigma}$ denotes the uniaxial tensile yield stress along the RD obtained from the virtual tests. The symbols “○” are the yield stress points obtained from the virtual laboratory simulations. The symbols “□” are the experimental data from Wu et al. (2003). Yld91, Yld2000-2D (for the plain stress state), and Yld2004-18p are the yield functions proposed by Barlat et al. (1991, 2003, 2005). Yld2004-27p is the yield function proposed by Aretz et al. (2010). The yield surfaces predicted by the identified Yld2004-18p, and Yld2004-27p yield functions are almost the same.

Figs. 16–19 show the yield surfaces predicted by all considered yield functions at equal normalized shear stress $\sigma_{12}/\bar{\sigma}$. Fig. 20 provides a direct comparison of the Yld2000-2D, Yld2004-18p, and Yld2004-27p yield functions. All the yield functions predict a higher maximum value of $\sigma_{12}/\bar{\sigma}$ for the hot-band case than for the cold-rolled case. This is consistent with the fact that the yield surfaces of the Cube and Goss orientations have a higher maximum $\sigma_{12}/\bar{\sigma}$ than the yield surfaces of the Copper, S, and Brass orientations (Barlat and Richmond, 1987). In contrast to the remaining yield functions, the Yld91 yield function overrates the effect of shear stress σ_{12} . Fig. 20 shows that the yield functions Yld2004-18p and Yld2004-27p predict a

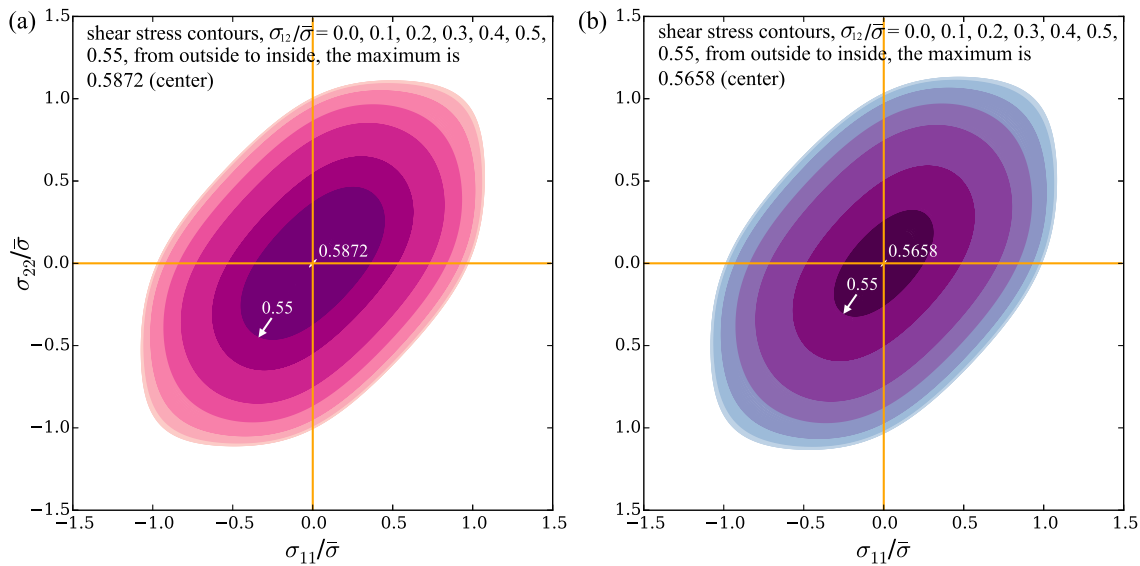


Fig. 16. Tricomponent (σ_{11} - σ_{22} - σ_{12}) yield surfaces with constant $\sigma_{12}/\bar{\sigma}$ contours of the hot-band (a) and the cold-rolled (b) samples predicted by the identified Yld91 yield function (Barlat et al., 1991). $\bar{\sigma}$ denotes the uniaxial tensile yield stress along the RD obtained from the virtual tests.

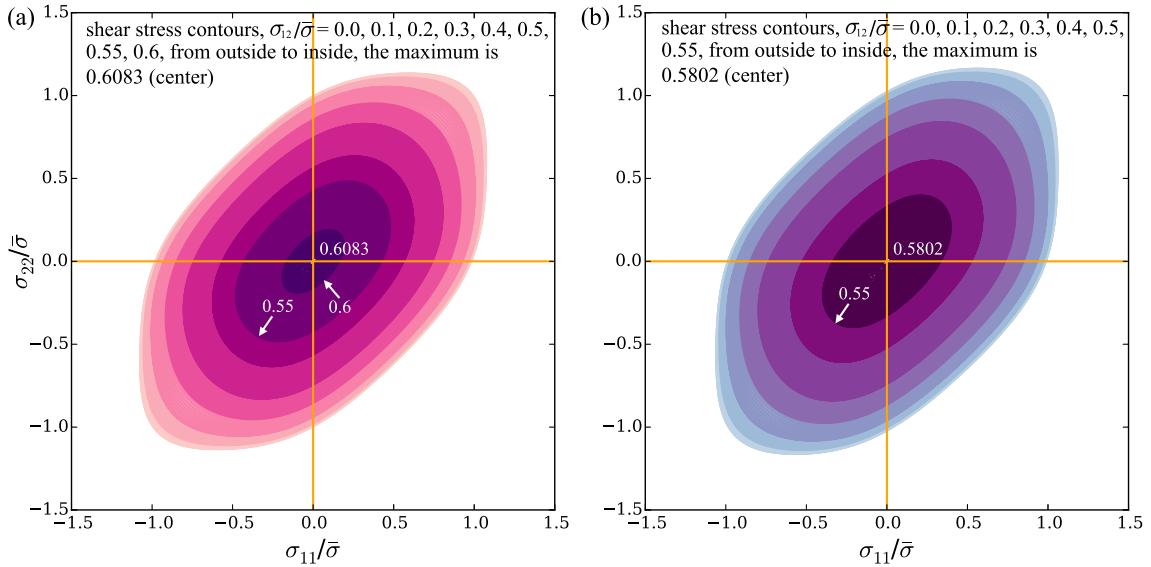


Fig. 17. Tricomponent (σ_{11} - σ_{22} - σ_{12}) yield surfaces with constant $\sigma_{12}/\bar{\sigma}$ contours of the hot-band (a) and the cold-rolled (b) samples predicted by the identified Yld2000-2D yield function (Barlat et al., 2003). $\bar{\sigma}$ denotes the uniaxial tensile yield stress along the RD obtained from the virtual tests.

perfectly consistent yield surface for both, the hot-band and the cold-rolled samples. While the prediction of the Yld2000-2D yield function differs slightly from the one obtained by the Yld2004-18p and Yld2004-27p functions.

As mentioned before, the hot-band sample was cold-rolled to 50% thickness reduction to arrive at the cold-rolled sample state. When the metal sheet is rolled, the grain re-orientation in the sheet induces orthotropy (Kowalczyk and Gambin, 2004), and it can be assumed that the same RD-TD-ND coordinate system can be used to plot the yield surfaces of both, the hot-band and the cold-rolled samples. During the rolling process, the yield surfaces will expand due to work hardening. As the same material parameters for both cases are used in this work for the CP model, here the yield surface expansion is not considered, and only the shape change of the yield surface from the hot-band sample to the cold-rolled sample can be discussed. Fig. 21 shows the comparison of yield surfaces predicted by the Yld2004-18p yield function for both, the hot-band and the cold-rolled samples. It can be observed, that the increased value of uniaxial tensile yield stress in the TD ($\theta = 90^\circ$) is slightly higher than that in the RD ($\theta = 0^\circ$). Looking back at the $Y_\theta - \theta$ curves in Fig. 10, Y_θ in the TD is slightly higher than 1.0, which is consistent with Fig. 21.

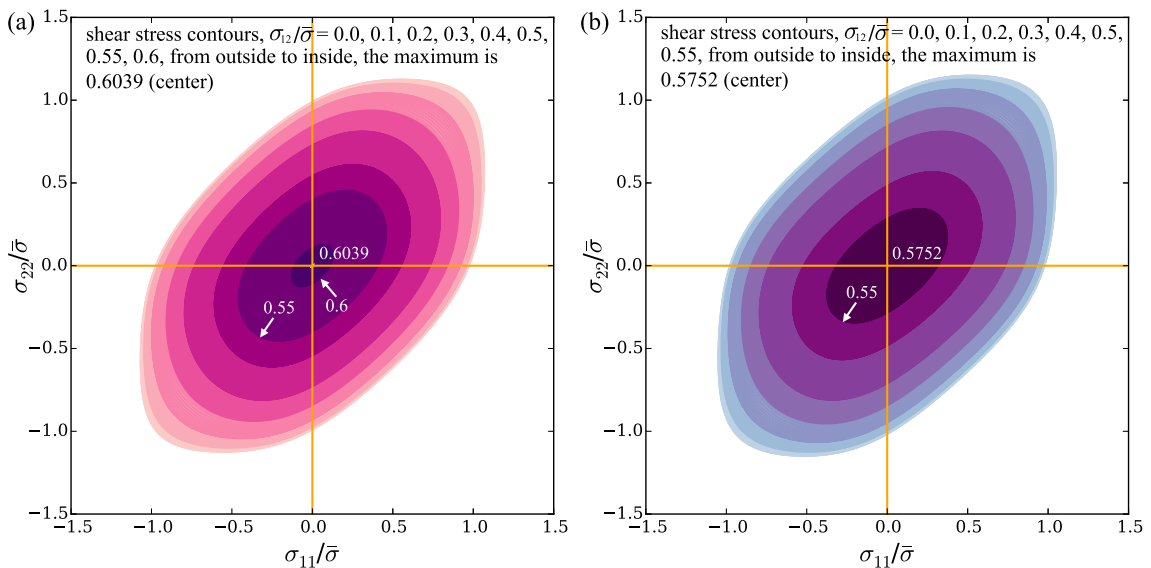


Fig. 18. Tricomponent (σ_{11} - σ_{22} - σ_{12}) yield surfaces with constant $\sigma_{12}/\bar{\sigma}$ contours of the hot-band (a) and the cold-rolled (b) samples predicted by the identified Yld2004-18p yield function (Barlat et al., 2005). $\bar{\sigma}$ denotes the uniaxial tensile yield stress along the RD obtained from the virtual tests.

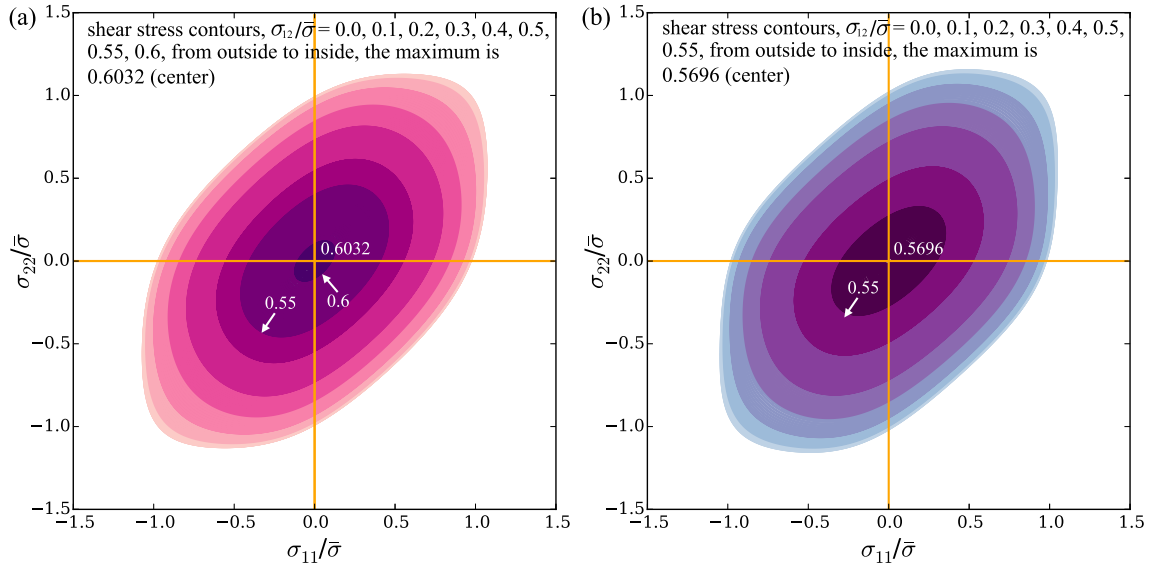


Fig. 19. Tricomponent (σ_{11} - σ_{22} - σ_{12}) yield surfaces with constant $\sigma_{12}/\bar{\sigma}$ contours of the hot-band (a) and cold-rolled (b) samples predicted by the identified Yld2004-27p yield function (Aretz et al., 2010). $\bar{\sigma}$ denotes the uniaxial tensile yield stress along the RD obtained from the virtual tests.

Advanced yield functions (Karafillis and Boyce, 1993; Barlat et al., 1997, 2005; Yoon et al., 2006, 2014) generally use both, uniaxial tensile yield stresses and r -values, simultaneously as an input and, therefore, usually show good predictions of the r -values and the normalized yield stresses. To some extent the predicted yield surfaces obtained by using different yield functions show remarkably different performances (Lademo et al., 1999; Wu et al., 2003; Mattiasson and Sigvant, 2008; Rabahallah et al., 2009; Aretz and Barlat, 2013). In addition, some yield functions identified using r -values provides a good description of the r -values but a relatively poor reproduction of the yield stress anisotropy, and vice versa. The deformation modes occurring during sheet metal forming are far more complex than those during uniaxial tension and usually also vary during subsequent forming operations. It is therefore difficult to conclude, whether the yield functions identified by the limited uniaxial tensile tests will also perform well in the complex deformation modes. With the virtual laboratory presented here, a large number of supplementing deformation modes can be used to identify parameters for advanced yield functions in

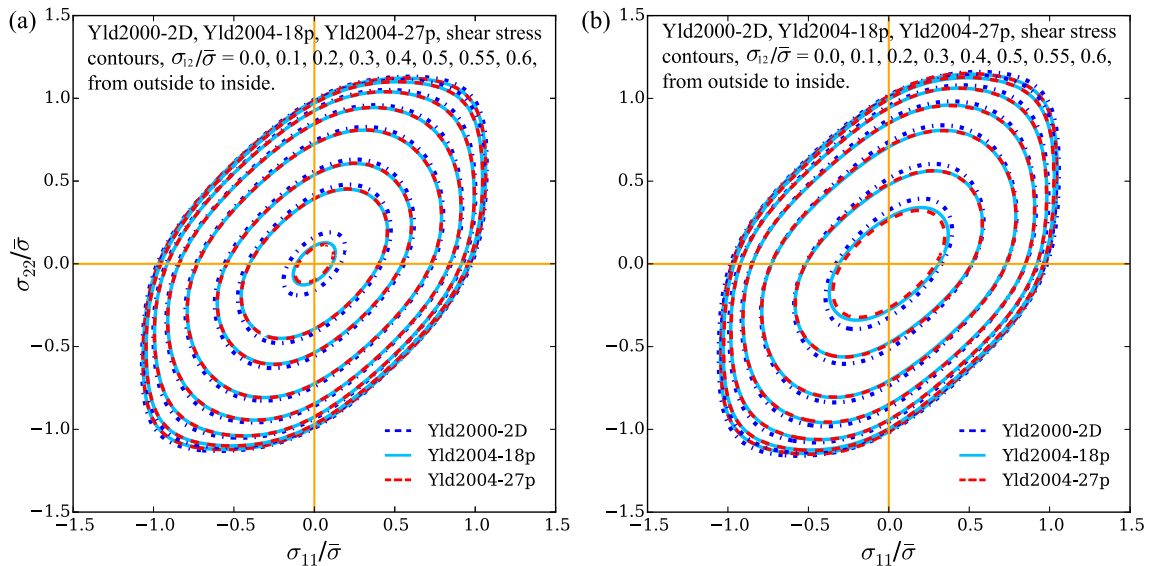


Fig. 20. Tricomponent (σ_{11} - σ_{22} - σ_{12}) yield surfaces with constant $\sigma_{12}/\bar{\sigma}$ contours of the hot-band (a) and the cold-rolled (b) AA3104 aluminum alloy predicted by the identified Yld2000-2D (Barlat et al., 2003), Yld2004-18p (Barlat et al., 2005) and Yld2004-27p (Aretz et al., 2010) yield functions. $\bar{\sigma}$ denotes the uniaxial tensile yield stress along the RD obtained from the virtual tests. The predicted tricomponent yield surfaces are almost the same for both two cases of AA3104 aluminum alloy, especially, the tricomponent yield surfaces predicted by the Yld2004-18p and Yld2004-27p yield functions for both cases are nearly exactly the same.

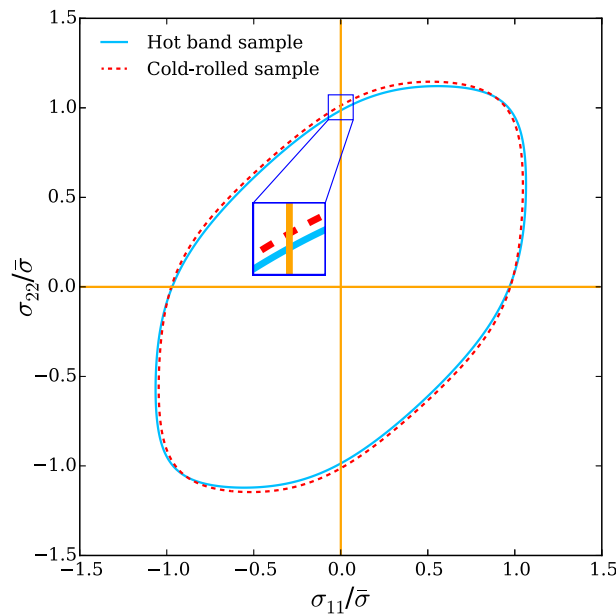


Fig. 21. The shape change of the yield surfaces ($\sigma_{12} = 0$) from the hot-band sample to the cold-rolled sample. Both two yield surfaces are predicted by the identified Yld2004-18p yield function (Barlat et al., 2005).

order to identify appropriate sets of suited parameters that match all deformation modes. The identified yield functions, except Yld91, all show good and actually almost the same performance in fitting yield surfaces, predicting the strength anisotropy and the deformation anisotropy which are related to the gradients of yield surfaces.

6.3. Convexity of the yield surfaces predicted by the virtual laboratory

The convexity of yield surfaces or yield functions, which is required according to the DRUCKER's postulate, is a crucial element for conducting nonlinear finite element analysis. Non-convexity of a yield function is likely to cause numerical difficulties in terms of non-uniqueness or singularity. Also, single crystalline yield surfaces constructed of dislocation slip systems are generally convex (Raabe et al., 2002a). Although in the current study most of the stress points are well enclosed by the four identified yield functions, it is pertinent to note that a set of scattered probed stress points, derived from full-field simulations, is located inside of the fitted convex yield surface hull, as shown in Figs. 14 and 15. In the biaxial tension loading state of the cold-rolled case, for example, some of the stress points with deformation modes approximating a near plane strain state, are apparently located inside the identified yield functions and deteriorate the convexity of the yield surfaces predicted by the virtual tests. In the view of the materials' intrinsic properties, the true local shapes of yield surfaces are governed by the crystallographic texture, grain morphology, slip anisotropy, self and latent hardening, dislocation patterns and substructures, as well as the phase distributions to name but a few essential microstructure effects. We therefore assume that the scatter of the stress points and the partial non-convexity of the yield surfaces result from the combined effects of the numerical approximations, the representation and discretization of the polycrystalline microstructure in the underlying full-field simulations, as well as the microscopic plastic deformation mechanisms adopted in the present CP model.

An important feature of deformed polycrystals is that their plastic deformation field is highly inhomogeneous (Sachtleber et al., 2002; Zhao et al., 2008). The crystallographic texture and the grain morphology result in a significant inter-granular and intra-granular inhomogeneous distributions of stress and strain, as exemplified in Fig. 22, which shows the cold-rolled sample after uniaxial tension along the direction 45° to the RD. High resolution CP simulations are capable of mapping such inhomogeneities and hence provide a more authentic description of the micromechanics of polycrystalline matter as opposed to conventional homogenization models (Sachtleber et al., 2002; Zhao et al., 2008; Tasan et al., 2014a,b). In cases of the occurrence of such substantial local inhomogeneities in the underlying full-field simulations, corresponding yield points may deviate from prescribed fitting functions, leading to a local non-convexity (Hu et al., 2015). Furthermore, as the global mechanical response of the RVEs is determined from the average of the behavior of single grains, the obvious difference of the mechanical response of these single grains may increase the numerical errors and then increase the scatter of the yield stress points. Certainly, this statistical discrepancy can be reduced by increasing the number of grains (*i.e.*, discrete orientations) in the RVEs.

Generally, the non-convexity problem would occur for a sharp texture or a single component texture, and such non-convexity is more significant for a rate insensitive model, as elaborated in the work of Savoie and MacEwen (1996). As a

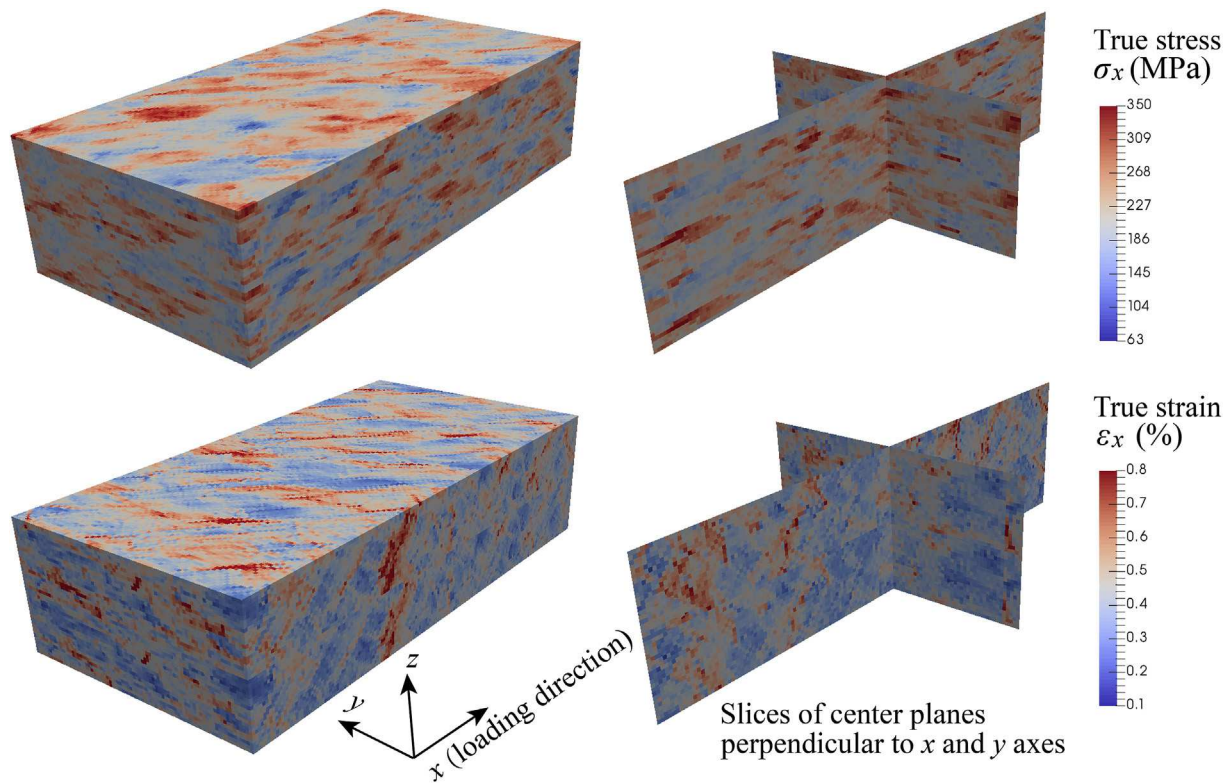


Fig. 22. Stress and strain field fluctuations of a cold-rolled sample after the uniaxial tension along the direction with 45° to the RD. The average nominal strain is 0.35%, corresponding to a plastic work of about 1 MPa. The RVE used is the one labelled as $\theta = 45^\circ$ in Fig. 7(c). A significant inter-granular and intra-granular inhomogeneous distribution of stress and strain is depicted by the high resolution CP simulation.

rate sensitive plastic flow law which is able to smoothen the sharp corners of yield surfaces was used in the present work, no sharp corners are observed in the yield surfaces of both, the hot-band and cold-rolled cases. The sharp textures shown in Figs. 4 and 5 have a significant effect on the scatter of stress points in the plane strain sections. Corresponding examples are the yield loci in the $\sigma_{11} - \sigma_{22}$ plane of the typical cold-rolling texture components of aluminum alloys, *i.e.*, the Cu, Brass, and S orientations, which show a quite flat section near the plane strain state and a “nose” near the equi-biaxial tension state (Barlat and Richmond, 1987). Such flat portions of the yield loci interfere with the convexity requirement of yield surfaces for example in near-plane strain regions as shown in Fig. 15.

For the texture-based yield function identification approaches, Rabahallah et al. (2009) stated that the unrealistic distortion of the yield surface can be prevented by using of numerous, evenly distributed, and equally weighted stress reference points. Gawad et al. (2015) suggested that optimizing the distribution of the yield stress points is important for the identification of yield functions like Yld2004-18p by using a least squares method. Hence, instead of using numerous arbitrarily selected stress points (Grytten et al., 2008; Rabahallah et al., 2009; Zhang et al., 2015a), Gawad et al. (2015) reduced the number of virtual experiments by means of a targeted selection, and also yielded a good performance. Therefore, optimizing the location of the yield stress points, especially in the region of biaxial tension, is expected to improve the yield surfaces predicted by the present virtual laboratory.

Given the high sensitivity of the r -values on the gradient of the yield surface, the partial non-convexity of the yield surfaces may lead to the possible local artificial variations of the r -values in dependence of the uniaxial tensile direction. As shown in Fig. 12, the r -values obtained from the virtual laboratory decrease monotonically with the tensile direction θ for θ below 30° , and there is a plateau in the range from $\theta = 52.5^\circ$ to $\theta = 60^\circ$. Although these features are not critical, they are a slightly different from the experimental results.

However, we believe the above features do not represent a shortcoming of our current high resolution CP based virtual laboratory approach, as these scattered yield stress points and the local non-convexity of yield surfaces are also frequently observed in mechanical tests (Barlat et al., 1997; Wu et al., 2003; Yoon et al., 2004; Wang et al., 2009; Khan et al., 2010) and virtual tests (Yoon et al., 2014; Kabirian and Khan, 2015) owing to the inherently inhomogeneous nature of the plastic deformation of polycrystalline matter. Furthermore, as the yield functions studied in this work are always convex, it can be figured out that the identified yield functions are reliable and robust to be used in simulations of sheet metal forming processes. Nevertheless, when the partial non-convexity of the yield surfaces or, equivalently, the scatter of the yield stress

points is too severe, it may deteriorate the convergence of the NLSM and render it challenging to identify adequate fitting parameters. In the present work, however, the parameters fitting process is robust even for a large number of yield stress points. This is attributed to the robustness of the LEVENBERG–MARQUARDT optimization algorithm adopted with the analytical Jacobian matrix. The algorithm is well known for its capability of finding a solution in many cases even if it starts very far off the final minimum.

In summary, the comparison with the full-field CP simulations which were referred here to as virtual tests and also with existing experimental data, supports the conclusion that the virtual laboratory introduced in this work is capable of properly describing, fitting, and reproducing the mechanical anisotropy of metals subjected to sheet metal forming operations. The methodology presented here relieves the trade-off of engineering forming simulations between accuracy and fitting effort, *i.e.*, it is often more practical to use a yield function with less fitting parameters owing to the limited accessible mechanical tests and the efforts associated with identifying those parameters. Moreover, as future extension, it is also possible to study the influence of strain path changes on the determined yield loci. However, this might require to use one of the more advanced CP constitutive models implemented in DAMASK which are capable of reproducing some of the mechanisms associated with complex strain path changes such as the multi-axial BAUSCHINGER effect.

7. Conclusions

A virtual laboratory approach, based on simulating plastic deformation by using highly resolved full-field crystal plasticity (CP) models with a spectral method is presented here, with the aim to predict the yield surface of polycrystalline materials. The approach is based on determining the response of microstructure models under various loading conditions. Its integration into the DAMASK multiphysics modeling package allows to use various advanced CP constitutive formulations. We apply this virtual laboratory concept to investigate the mechanical anisotropy of an AA3104 aluminum alloy with two different initial textures, *i.e.*, a recrystallization texture obtained from a commercially produced hot-band and a corresponding cold-rolling texture. The parameters of four yield functions frequently used in sheet metal forming, *e.g.*, Yld91, Yld2000-2D, Yld2004-18p, and Yld2004-27p, were determined for both states of the AA3104 aluminum alloy.

A large number of virtual tests with randomly generated deformation modes were performed by using the virtual laboratory. The predicted yield stress points were used to identify the parameters of the yield functions. In addition, uniaxial tensile tests in different directions were also performed by using the virtual laboratory to obtain both, the deformation anisotropy (r -values) and the strength anisotropy (normalized yield stresses, Y_θ). The results of virtual uniaxial tension demonstrate that the virtual laboratory is capable of replacing the mechanical tests that are typically required to extract the r -values and Y_θ . Although only yield stresses but no r -value and Y_θ values were used to identify the parameters, the identified yield functions, *i.e.*, Yld2000-2D, Yld2004-18p, and Yld2004-27p show good performance in fitting the yield surfaces, r -values, and Y_θ simultaneously. In contrast, the Yld91 yield function, due to a smaller number of required parameters, shows good performance in fitting yield surfaces but relatively poor capability in the prediction of r -values and Y_θ . The virtual laboratory simulations and the experimental results show that the presented approach, which combines both accuracy and efficiency, is a promising micromechanical-based tool for the investigation of mechanical anisotropy of metals and for the parameter identification of advanced yield functions.

The approach also shows that an efficient multiscale modeling connection can be established between full-field physically based constitutive CP modeling on the one hand and engineering anisotropy simulations on the other hand by using the open source DAMASK toolbox (<http://damask.mpie.de/>). This type of scale bridging simulation is important since sheet metal forming simulations that are based on yield surface functions must be designed in a way that allows users to fit them to the underlying physics that governing plastic deformation of complex engineering materials. In this study we have shown that this type of cross-scale simulation fulfills the requirement to fit arbitrary yield function parameters by using any kind of specific constitutive CP models that considers complex textures and adequately reflects the underlying deformation mechanisms.

Acknowledgments

This research was carried out under project number M41.2.10410 in the framework of the Research Program of the Material innovation institute (M2i) (www.m2i.nl). The financial support of M2i is gratefully acknowledged.

Appendix A. Rotation of orientations

As shown in Fig. 2, the transformation form $[XYZ]$ (*i.e.*, [RD-TD-ND]) to $[xyz]$ is written as $[xyz] = \mathbf{Q} \cdot [XYZ]$, and \mathbf{Q} is the transformation matrix, which can be expressed by the crystal orientation $\{\varphi_1, \Phi, \varphi_2\}$ using the BUNGE's convention (Bunge, 1982) of the EULER notation as:

$$\mathbf{Q} = \begin{bmatrix} \cos \phi_2 & \sin \phi_2 & 0 \\ -\sin \phi_2 & \cos \phi_2 & 0 \\ 0 & 0 & 1 \end{bmatrix} \begin{bmatrix} 1 & 0 & 0 \\ 0 & \cos \Phi & \sin \Phi \\ 0 & -\sin \Phi & \cos \Phi \end{bmatrix} \begin{bmatrix} \cos \varphi_1 & \sin \varphi_1 & 0 \\ -\sin \varphi_1 & \cos \varphi_1 & 0 \\ 0 & 0 & 1 \end{bmatrix} \quad (\text{A.1})$$

Similarly, the transformation matrix \mathbf{R} between $[XYZ]$ and $[X'Y'Z']$ is:

$$[X'Y'Z'] = \mathbf{R} \cdot [XYZ], \quad \text{with } \mathbf{R} = \begin{bmatrix} \cos \theta & \sin \theta & 0 \\ -\sin \theta & \cos \theta & 0 \\ 0 & 0 & 1 \end{bmatrix} \quad (\text{A.2})$$

As a result, the transformation form $[X'Y'Z']$ to $[xyz]$ is $[xyz] = \mathbf{Q} \cdot \mathbf{R}^T \cdot [X'Y'Z']$, then the orientation of grains in the new axes $[X'Y'Z']$ is $\{\varphi_1 - \theta, \phi, \varphi_2\}$.

References

- Alankar, A., Eisenlohr, P., Raabe, D., 2011. A dislocation density-based crystal plasticity constitutive model for prismatic slip in α -titanium. *Acta Mater.* 59 (18), 7003–7009. <http://dx.doi.org/10.1016/j.actamat.2011.07.053>.
- Aretz, H., Aegerter, J., Engler, O., 2010. Analysis of earing in deep drawn cups. *AIP Conf. Proc.* 1252 (1), 417–424. <http://dx.doi.org/10.1063/1.3457585>.
- Aretz, H., Barlat, F., 2013. New convex yield functions for orthotropic metal plasticity. *Int. J. Non-Linear Mech.* 51, 97–111. <http://dx.doi.org/10.1016/j.jnonlinmec.2012.12.007>.
- Arminjon, M., Bacroix, B., 1991. On plastic potentials for anisotropic metals and their derivation from the texture function. *Acta Mech.* 88 (3–4), 219–243. <http://dx.doi.org/10.1007/BF01177098>.
- Balay, S., Brown, J., Buschelman, K., Eijkhout, V., Gropp, W.D., Kaushik, D., Knepley, M.G., McInnes, L.C., Smith, B.F., Zhang, H., 2013. *PETSc Users Manual*. Technical report.
- Banabic, D., Kuwabara, T., Balan, T., Comsa, D.S., Julean, D., 2003. Non-quadratic yield criterion for orthotropic sheet metals under plane-stress conditions. *Int. J. Mech. Sci.* 45 (5), 797–811. [http://dx.doi.org/10.1016/S0020-7403\(03\)00139-5](http://dx.doi.org/10.1016/S0020-7403(03)00139-5).
- Barlat, F., Chung, K., 2005. Anisotropic strain rate potential for aluminum alloy plasticity. In: Banabic, D. (Ed.), *Proceedings of the 8th ESAFORM Conference on Material Forming*. The Publishing House of the Romanian Academy, Bucharest, pp. 415–418. Cluj-Napoca, Romania.
- Barlat, F., Lian, K., 1989. Plastic behavior and stretchability of sheet metals. Part I: a yield function for orthotropic sheets under plane stress conditions. *Int. J. Plast.* 5 (1), 51–66. [http://dx.doi.org/10.1016/0749-6419\(89\)90019-3](http://dx.doi.org/10.1016/0749-6419(89)90019-3).
- Barlat, F., Richmond, O., 1987. Prediction of tricomponent plane stress yield surfaces and associated flow and failure behavior of strongly textured f.c.c. polycrystalline sheets. *Mater. Sci. Eng.* 95, 15–29. [http://dx.doi.org/10.1016/0025-5416\(87\)90494-0](http://dx.doi.org/10.1016/0025-5416(87)90494-0).
- Barlat, F., Lege, D.J., Brem, J.C., 1991. A six-component yield function for anisotropic materials. *Int. J. Plast.* 7 (7), 693–712. [http://dx.doi.org/10.1016/0749-6419\(91\)90052-Z](http://dx.doi.org/10.1016/0749-6419(91)90052-Z).
- Barlat, F., Maeda, Y., Chung, K., Yanagawa, M., Brem, J.C., Hayashida, Y., Lege, D.J., Matsui, K., Murtha, S.J., Hattori, S., Becker, R.C., Makosey, S., 1997. Yield function development for aluminum alloy sheets. *J. Mech. Phys. Solids* 45 (11–12), 1727–1763. [http://dx.doi.org/10.1016/S0022-5096\(97\)00034-3](http://dx.doi.org/10.1016/S0022-5096(97)00034-3).
- Barlat, F., Brem, J.C., Yoon, J.W., Chung, K., Dick, R.E., Lege, D.J., Pourboghrat, F., Choi, S.-H., Chu, E., 2003. Plane stress yield function for aluminum alloy sheets—part 1: theory. *Int. J. Plast.* 19 (9), 1297–1319. [http://dx.doi.org/10.1016/S0749-6419\(02\)00019-0](http://dx.doi.org/10.1016/S0749-6419(02)00019-0).
- Barlat, F., Aretz, H., Yoon, J.W., Karabin, M.E., Brem, J.C., Dick, R.E., 2005. Linear transformation-based anisotropic yield functions. *Int. J. Plast.* 21 (5), 1009–1039. <http://dx.doi.org/10.1016/j.jiplas.2004.06.004>.
- Barlat, F., Yoon, J.W., Cazacu, O., 2007. On linear transformations of stress tensors for the description of plastic anisotropy. *Int. J. Plast.* 23 (5), 876–896. <http://dx.doi.org/10.1016/j.jiplas.2006.10.001>.
- Beaudoin, A.J., Dawson, P.R., Mathur, K.K., Kocks, U.F., 1995. A hybrid finite element formulation for polycrystal plasticity with consideration of macrostructural and microstructural linking. *Int. J. Plast.* 11 (5), 501–521. [http://dx.doi.org/10.1016/S0749-6419\(99\)80003-5](http://dx.doi.org/10.1016/S0749-6419(99)80003-5).
- Beaudoin, A.J., Mecking, H., Kocks, U.F., 1996. Development of localized orientation gradients in fcc polycrystals. *Philos. Mag.* A 73 (6), 1503–1517. <http://dx.doi.org/10.1080/01418619608242998>.
- Bishop, J.F.W., Hill, R., 1951. A theory of the plastic distortion of a polycrystalline aggregate under combined stresses. *Philos. Mag.* 42 (327), 414–427. <http://dx.doi.org/10.1080/14786445108561065>.
- Brisard, S., Dormieux, L., 2010. FFT-based methods for the mechanics of composites: a general variational framework. *Comput. Mater. Sci.* 49 (3), 663–671. <http://dx.doi.org/10.1016/j.commatsci.2010.06.009>.
- Bron, F., Besson, J., 2004. A yield function for anisotropic materials: application to aluminum alloys. *Int. J. Plast.* 20 (4–5), 937–963. <http://dx.doi.org/10.1016/j.jiplas.2003.06.001>.
- Brown, S., Kim, K., Anand, L., 1989. An internal variable constitutive model for hot working of metals. *Int. J. Plast.* 5 (2), 95–130. [http://dx.doi.org/10.1016/0749-6419\(89\)90025-9](http://dx.doi.org/10.1016/0749-6419(89)90025-9).
- Bunge, H.J., 1982. *Texture Analysis in Materials Science*. Butterworths, London.
- Cazacu, O., Plunkett, B., Barlat, F., 2006. Orthotropic yield criterion for hexagonal closed packed metals. *Int. J. Plast.* 22 (7), 1171–1194. <http://dx.doi.org/10.1016/j.jiplas.2005.06.001>.
- Cereceda, D., Diehl, M., Roters, F., Raabe, D., Perlado, J.M., Marian, J., 2016. Unraveling the temperature dependence of the yield strength in single-crystal tungsten using atomistically-informed crystal plasticity calculations. *Int. J. Plast.* 78, 242–265.
- Choi, S.H., Brem, J.C., Barlat, F., Oh, K.H., 2000. Macroscopic anisotropy in AA5019A sheets. *Acta Mater.* 48 (8), 1853–1863. [http://dx.doi.org/10.1016/S1359-6454\(99\)00470-X](http://dx.doi.org/10.1016/S1359-6454(99)00470-X).
- Crumbach, M., Goerdeler, M., Gottstein, G., 2006. Modelling of recrystallisation textures in aluminium alloys: I. Model set-up and integration. *Acta Mater.* 54, 3275–3289. <http://dx.doi.org/10.1016/j.actamat.2006.03.017>.
- DAMASK. Düsseldorf Advanced Material Simulation Kit, 2014. URL <http://damask.mpij.de/>.
- Darrieulat, M., Piot, D., 1996. A method of generating analytical yield surfaces of crystalline materials. *Int. J. Plast.* 12 (5), 575–610. [http://dx.doi.org/10.1016/S0749-6419\(98\)80001-6](http://dx.doi.org/10.1016/S0749-6419(98)80001-6).
- Dawson, P.R., Boyce, D.E., Hale, R., Durkot, J.P., 2005. An isoparametric piecewise representation of the anisotropic strength of polycrystalline solids. *Int. J. Plast.* 21 (2), 251–283. <http://dx.doi.org/10.1016/j.jiplas.2003.11.020>.
- Delannay, L., Melchior, M.A., Signorelli, J.W., Remacle, J.F., Kuwabara, T., 2009. Influence of grain shape on the planar anisotropy of rolled steel sheets - evaluation of three models. *Comput. Mater. Sci.* 45 (3), 739–743. <http://dx.doi.org/10.1016/j.commatsci.2008.06.013>.
- Delannay, L., Barnett, M.R., 2012. Modelling the combined effect of grain size and grain shape on plastic anisotropy of metals. *Int. J. Plast.* 32–33, 70–84. <http://dx.doi.org/10.1016/j.jiplas.2011.12.002>.
- Eisenlohr, P., Roters, F., 2008. Selecting sets of discrete orientations for accurate texture reconstruction. *Comput. Mater. Sci.* 42 (4), 670–678. <http://dx.doi.org/10.1016/j.commatsci.2007.09.015>.
- Eisenlohr, P., Diehl, M., Lebensohn, R.A., Roters, F., 2013. A spectral method solution to crystal elasto-viscoplasticity at finite strains. *Int. J. Plast.* 46, 37–53. <http://dx.doi.org/10.1016/j.jiplas.2012.09.012>.
- Engler, O., Mertens, N., Van Dam, P., 2011. Texture-based design of a convoluted cut-edge for earing-free beverage cans. *J. Mater. Process. Technol.* 211 (7), 1278–1284. <http://dx.doi.org/10.1016/j.jmatprotec.2011.02.011>.
- Eyre, D.J., Milton, G.W., 1999. A fast numerical scheme for computing the response of composites using grid refinement. *Eur. Phys. J. Appl. Phys.* 6 (1), 41–47. <http://dx.doi.org/10.1051/epjap:1999150>.
- Gambin, W., 1991. Crystal plasticity based on yield surfaces with rounded-off corners. *Z. Angew. Math. Mech.* 71 (4), T265–T268.

- Gawad, J., Banabic, D., Bael, A.V., Comsa, D.S., Gologanu, M., Eyckens, P., Van Houtte, P., Roose, D., 2015. An evolving plane stress yield criterion based on crystal plasticity virtual experiments. *Int. J. Plast.* 75, 141–169. <http://dx.doi.org/10.1016/j.ijplas.2015.02.011>.
- Grytten, F., Holmedal, B., Hopperstad, O.S., Børvik, T., 2008. Evaluation of identification methods for YLD2004-18p. *Int. J. Plast.* 24 (12), 2248–2277. <http://dx.doi.org/10.1016/j.ijplas.2007.11.005>.
- Haouaoui, M., Karaman, I., Maier, H.J., 2006. Flow stress anisotropy and Bauschinger effect in ultrafine grained copper. *Acta Mater.* 54 (20), 5477–5488. <http://dx.doi.org/10.1016/j.actamat.2006.07.022>.
- Helm, D., Butz, A., Raabe, D., Gumbsch, P., 2011. Microstructure-based description of the deformation of metals: theory and application. *JOM* 63 (4), 26–33. <http://dx.doi.org/10.1007/s11837-011-0056-8>.
- Hill, R., 1948. A theory of the yielding and plastic flow of anisotropic metals. *Proc. R. Soc. A Math. Phys. Eng. Sci.* 193 (1033), 281–297. <http://dx.doi.org/10.1098/rspa.1948.0045>.
- Hill, R., 1965. Continuum micro-mechanics of elastoplastic polycrystals. *J. Mech. Phys. Solids* 13 (2), 89–101. [http://dx.doi.org/10.1016/0022-5096\(65\)90023-2](http://dx.doi.org/10.1016/0022-5096(65)90023-2).
- Hill, R., 1979. Theoretical plasticity of textured aggregates. *Math. Proc. Camb. Philos. Soc.* 85 (01), 179. <http://dx.doi.org/10.1017/S0305004100055596>.
- Hill, R., 1990. Constitutive modelling of orthotropic plasticity in sheet metals. *J. Mech. Phys. Solids* 38 (3), 405–417. [http://dx.doi.org/10.1016/0022-5096\(90\)90006-P](http://dx.doi.org/10.1016/0022-5096(90)90006-P).
- Hölscher, M., Raabe, D., Lücke, K., 1991. Rolling and recrystallization textures of bcc steels. *Steel Res. Int.* 62 (12), 567–575.
- Hölscher, M., Raabe, D., Lücke, K., 1994. Relationship between rolling textures and shear textures in f.c.c. and b.c.c. metals. *Acta Metall. Mater.* 42 (3), 879–886. [http://dx.doi.org/10.1016/0956-7151\(94\)90283-6](http://dx.doi.org/10.1016/0956-7151(94)90283-6).
- Honneff, H., Mecking, H., 1981. Analysis of the deformation texture at different rolling conditions. In: *Proc. 6th Int. Conf. on Texture of Materials (ICOTOM-6)*, vol. 1. The Iron and Steel Institute of Japan, Tokyo, pp. 347–355.
- Hosford, W.F., 1972. A generalized isotropic yield criterion. *J. Appl. Mech.* 39 (2), 607–609. <http://dx.doi.org/10.1115/1.3422732>.
- Hosford, W.F., 1985. Comments on anisotropic yield criteria. *Int. J. Mech. Sci.* 27 (7–8), 423–427. [http://dx.doi.org/10.1016/0020-7403\(85\)90032-3](http://dx.doi.org/10.1016/0020-7403(85)90032-3).
- Hosford, W.F., 1988. Limitations of non-quadratic anisotropic yield criteria and their use in analysis of sheet forming. In: *International Deep Drawing Research Group (Ed.), ASM International: North American Deep Drawing Research Group*, pp. 163–170.
- Hu, G., Huang, S., Lu, D., Zhong, X., Li, Z., Brocks, W., Zhang, K., 2015. Subsequent yielding of polycrystalline aluminum after cyclic tension-compression analyzed by experiments and simulations. *Int. J. Solids Struct.* 56–57, 142–153. <http://dx.doi.org/10.1016/j.ijsolstr.2014.11.022>.
- Hutchinson, J.W., 1976. Bounds and self-consistent estimates for creep of polycrystalline materials. *Proc. R. Soc. A* 348, 101–127. <http://dx.doi.org/10.1098/rspa.1976.0027>.
- Kabirian, F., Khan, A.S., 2015. Anisotropic yield criteria in σ - τ stress space for materials with yield asymmetry. *Int. J. Solids Struct.* 67–68, 116–126. <http://dx.doi.org/10.1016/j.ijsolstr.2015.04.006>.
- Kanjarla, A.K., Van Houtte, P., Delannay, L., 2010. Assessment of plastic heterogeneity in grain interaction models using crystal plasticity finite element method. *Int. J. Plast.* 26 (8), 1220–1233. <http://dx.doi.org/10.1016/j.ijplas.2009.05.005>.
- Kanjarla, A.K., Lebensohn, R.A., Balogh, L., Tomé, C.N., 2012. Study of internal lattice strain distributions in stainless steel using a full-field elasto-viscoplastic formulation based on fast Fourier transforms. *Acta Mater.* 60 (6–7), 3094–3106. <http://dx.doi.org/10.1016/j.actamat.2012.02.014>.
- Karafilis, A.P., Boyce, M.C., 1993. A general anisotropic yield criterion using bounds and a transformation weighting tensor. *J. Mech. Phys. Solids* 41 (12), 1859–1886. [http://dx.doi.org/10.1016/0022-5096\(93\)90073-O](http://dx.doi.org/10.1016/0022-5096(93)90073-O).
- Khan, A.S., Pandey, A., Stoughton, T., 2010. Evolution of subsequent yield surfaces and elastic constants with finite plastic deformation. Part III: yield surface in tension-tension stress space (Al 6061-T 6511 and annealed 1100 Al. *Int. J. Plast.* 26 (10), 1432–1441. <http://dx.doi.org/10.1016/j.ijplas.2009.07.007>.
- Knezevic, M., McCabe, R.J., Tomé, C.N., Lebensohn, R.A., Chen, S.R., Cady, C.M., Gray III, G.T., Mihaila, B., 2013. Modeling mechanical response and texture evolution of α -uranium as a function of strain rate and temperature using polycrystal plasticity. *Int. J. Plast.* 43, 70–84. <http://dx.doi.org/10.1016/j.ijplas.2012.10.011>.
- Kocks, U.F., 1958. Polyslip in polycrystals. *Acta Metall.* 6 (2), 85–94. [http://dx.doi.org/10.1016/0001-6160\(58\)90117-2](http://dx.doi.org/10.1016/0001-6160(58)90117-2).
- Kocks, U.F., Chandra, H., 1982. Slip geometry in partially constrained deformation. *Acta Metall.* 30 (3), 695–709. [http://dx.doi.org/10.1016/0001-6160\(82\)90119-5](http://dx.doi.org/10.1016/0001-6160(82)90119-5).
- Kowalczyk, K., Gambin, W., 2004. Model of plastic anisotropy evolution with texture-dependent yield surface. *Int. J. Plast.* 20 (1), 19–54. [http://dx.doi.org/10.1016/S0749-6419\(03\)00010-X](http://dx.doi.org/10.1016/S0749-6419(03)00010-X).
- Kraska, M., Doig, M., Tikhomirov, D., Raabe, D., Roters, F., 2009. Virtual material testing for stamping simulations based on polycrystal plasticity. *Comput. Mater. Sci.* 46 (2), 383–392. <http://dx.doi.org/10.1016/j.commatsci.2009.03.025>.
- Kröner, E., 1958. Berechnung der elastischen Konstanten des Vielkristalls aus den Konstanten des Einkristalls. *Z. für Phys.* 151 (4), 504–518. <http://dx.doi.org/10.1007/BF01337948>.
- Lademo, O.G., Hopperstad, O.S., Langseth, M., 1999. An evaluation of yield criteria and flow rules for aluminium alloys. *Int. J. Plast.* 15 (2), 191–208. [http://dx.doi.org/10.1016/S0749-6419\(98\)00064-3](http://dx.doi.org/10.1016/S0749-6419(98)00064-3).
- Lademo, O.G., Engler, O., Keller, S., Berstad, T., Pedersen, K.O., Hopperstad, O.S., 2009. Identification and validation of constitutive model and fracture criterion for AlMgSi alloy with application to sheet forming. *Mater. Des.* 30 (8), 3005–3019. <http://dx.doi.org/10.1016/j.matdes.2008.12.020>.
- Lebensohn, R.A., 2001. N-site modeling of a 3D viscoplastic polycrystal using fast Fourier transform. *Acta Mater.* 49 (14), 2723–2737. [http://dx.doi.org/10.1016/S1359-6454\(01\)00172-0](http://dx.doi.org/10.1016/S1359-6454(01)00172-0).
- Lebensohn, R.A., Tomé, C.N., 1993. A study of the stress state associated with twin nucleation and propagation in anisotropic materials. *Philos. Mag. A* 67 (1), 187–206. <http://dx.doi.org/10.1080/01418619308207151>.
- Lebensohn, R.A., Tomé, C.N., 1994. A self-consistent viscoplastic model: prediction of rolling textures of anisotropic polycrystals. *Mater. Sci. Eng. A* 175 (1–2), 71–82. [http://dx.doi.org/10.1016/0921-5093\(94\)91047-2](http://dx.doi.org/10.1016/0921-5093(94)91047-2).
- Lebensohn, R.A., González, M.I., Tomé, C.N., Pochettino, A.A., 1996. Measurement and prediction of texture development during a rolling sequence of Zircaloy-4 tubes. *J. Nucl. Mater.* 229, 57–64. [http://dx.doi.org/10.1016/0022-3115\(95\)00210-3](http://dx.doi.org/10.1016/0022-3115(95)00210-3).
- Lebensohn, R.A., Wenk, H.-R., Tomé, C.N., 1998. Modelling deformation and recrystallization textures in calcite. *Acta Mater.* 46 (8), 2683–2693. [http://dx.doi.org/10.1016/S1359-6454\(97\)00477-1](http://dx.doi.org/10.1016/S1359-6454(97)00477-1).
- Lebensohn, R.A., Kanjarla, A.K., Eisenlohr, P., 2012. An elasto-viscoplastic formulation based on fast Fourier transforms for the prediction of micromechanical fields in polycrystalline materials. *Int. J. Plast.* 32–33, 59–69. <http://dx.doi.org/10.1016/j.ijplas.2011.12.005>.
- Lee, S.-B., Lebensohn, R.A., Rollett, A.D., 2011. Modeling the viscoplastic micromechanical response of two-phase materials using Fast Fourier Transforms. *Int. J. Plast.* 27 (5), 707–727. <http://dx.doi.org/10.1016/j.ijplas.2010.09.002>.
- Levenberg, K., 1944. A method for the solution of certain problems in least squares. *Q. Appl. Math.* 2, 164–168.
- Li, S., Hoferlin, E., Van Bael, A., Van Houtte, P., Teodosiu, C., 2003. Finite element modeling of plastic anisotropy induced by texture and strain-path change. *Int. J. Plast.* 19 (5), 647–674. [http://dx.doi.org/10.1016/S0749-6419\(01\)00079-1](http://dx.doi.org/10.1016/S0749-6419(01)00079-1).
- Liu, B., Raabe, D., Roters, F., Eisenlohr, P., Lebensohn, R.A., 2010. Comparison of finite element and fast Fourier transform crystal plasticity solvers for texture prediction. *Model. Simul. Mater. Sci. Eng.* 18 (8), 085005. <http://dx.doi.org/10.1088/0965-0393/18/8/085005>.
- Ma, A., Roters, F., 2004. A constitutive model for fcc single crystals based on dislocation densities and its application to uniaxial compression of aluminium single crystals. *Acta Mater.* 52 (12), 3603–3612. <http://dx.doi.org/10.1016/j.actamat.2004.04.012>.
- Marquardt, D.W., 1963. An algorithm for least-squares estimation of nonlinear parameters. *J. Soc. Ind. Appl. Math.* 11 (2), 431–441. <http://dx.doi.org/10.1137/0111030>.
- Mattiasson, K., Sigvant, M., 2008. An evaluation of some recent yield criteria for industrial simulations of sheet forming processes. *Int. J. Mech. Sci.* 50 (4), 774–787. <http://dx.doi.org/10.1016/j.ijmecsci.2007.11.002>.

- Michel, J.C., Moulinec, H., Suquet, P., 2001. A computational scheme for linear and non-linear composites with arbitrary phase contrast. *Int. J. Numer. Methods Eng.* 52 (12), 139–160. <http://dx.doi.org/10.1002/nme.275>.
- Molinari, A., Canova, G.R., Ahzi, S., 1987. A self-consistent approach of the large deformation polycrystal viscoplasticity. *Acta Metall.* 35 (12), 2983–2994. [http://dx.doi.org/10.1016/0001-6160\(87\)90297-5](http://dx.doi.org/10.1016/0001-6160(87)90297-5).
- Monchiet, V., Bonnet, G., 2012. A polarization-based FFT iterative scheme for computing the effective properties of elastic composites with arbitrary contrast. *Int. J. Numer. Methods Eng.* 89 (11), 1419–1436. <http://dx.doi.org/10.1002/nme.3295>.
- Moulinec, H., Suquet, P., 1994. A fast numerical method for computing the linear and nonlinear properties of composites. *Comptes rendus l'Acad. Sci. Série II Méc. phys. chimie astron.* 318, 1417–1423.
- Mura, T., 1987. *Micromechanics of Defects in Solids*, second ed. Martinus Nijhoff Publishers, Dordrecht.
- Peirce, D., Asaro, R.J., Needleman, A., 1982. An analysis of nonuniform and localized deformation in ductile single crystals. *Acta Metall.* 30 (6), 1087–1119. [http://dx.doi.org/10.1016/0001-6160\(82\)90005-0](http://dx.doi.org/10.1016/0001-6160(82)90005-0).
- Plunkett, B., Lebensohn, R.A., Cazacu, O., Barlat, F., 2006. Anisotropic yield function of hexagonal materials taking into account texture development and anisotropic hardening. *Acta Mater.* 54 (16), 4159–4169. <http://dx.doi.org/10.1016/j.actamat.2006.05.009>.
- Prakash, A., Lebensohn, R.A., 2009. Simulation of micromechanical behavior of polycrystals: finite elements versus fast Fourier transforms. *Model. Simul. Mater. Sci. Eng.* 17, 064010–064016. <http://dx.doi.org/10.1088/0965-0393/17/6/064010>.
- Raabe, D., 1995a. Texture simulation for hot rolling of aluminium by use of a Taylor model considering grain interaction. *Acta Mater.* 43 (3), 1023–1028.
- Raabe, D., 1995b. Simulation of rolling textures of b.c.c. metals considering grain interactions and crystallographic slip on {110}, {112}, and {123} planes. *Mater. Sci. Eng. A* 197, 31–37.
- Raabe, D., 1995c. Investigation of contribution of {123} slip planes to development of rolling textures in bcc metals by use of Taylor models. *Mater. Sci. Technol.* 11 (5), 455–460.
- Raabe, D., 2000. Yield surface simulation for partially recrystallized aluminum polycrystals on the basis of spatially discrete data. *Comput. Mater. Sci.* 19 (1–4), 13–26. [http://dx.doi.org/10.1016/S0927-0256\(00\)00135-X](http://dx.doi.org/10.1016/S0927-0256(00)00135-X).
- Raabe, D., Roters, F., 2004. Using texture components in crystal plasticity finite element simulations. *Owen Richmond Memorial Special Issue Int. J. Plast.* 20 (3), 339–361. [http://dx.doi.org/10.1016/S0749-6419\(03\)00092-5](http://dx.doi.org/10.1016/S0749-6419(03)00092-5).
- Raabe, D., Sachtleber, M., Zhao, Z., Roters, F., Zaefferer, S., 2001. Micromechanical and macromechanical effects in grain scale polycrystal plasticity experimentation and simulation. *Acta Mater.* 49 (17), 3433–3441. [http://dx.doi.org/10.1016/S1359-6454\(01\)00242-7](http://dx.doi.org/10.1016/S1359-6454(01)00242-7).
- Raabe, D., Klose, P., Engl, B., Imlau, K.P., Friedel, F., Roters, F., 2002a. Concepts for integrating plastic anisotropy into metal forming simulations. *Adv. Eng. Mater.* 4 (4), 169–180. [http://dx.doi.org/10.1002/1527-2648\(200204\)4:4<169::AID-ADEM169>3.0.CO;2-G](http://dx.doi.org/10.1002/1527-2648(200204)4:4<169::AID-ADEM169>3.0.CO;2-G).
- Raabe, D., Zhao, Z., Mao, W., 2002b. On the dependence of in-grain subdivision and deformation texture of aluminum on grain interaction. *Acta Mater.* 50 (17), 4379–4394. [http://dx.doi.org/10.1016/S1359-6454\(02\)00276-8](http://dx.doi.org/10.1016/S1359-6454(02)00276-8).
- Raabe, D., Sachtleber, M., Weiland, H., Scheele, G., Zhao, Z., 2003. Grain-scale micromechanics of polycrystal surfaces during plastic straining. *Acta Mater.* 51, 1539–1560. [http://dx.doi.org/10.1016/S1359-6454\(02\)00557-8](http://dx.doi.org/10.1016/S1359-6454(02)00557-8).
- Rabahallah, M., Balan, T., Bouvier, S., Bacroix, B., Barlat, F., Chung, K., Teodosiu, C., 2009. Parameter identification of advanced plastic strain rate potentials and impact on plastic anisotropy prediction. *Int. J. Plast.* 25 (3), 491–512. <http://dx.doi.org/10.1016/j.ijplas.2008.03.006>.
- Raphanel, J.L., Van Houtte, P., 1985. Simulation of the rolling textures of b.c.c. metals by means of the relaxed Taylor theory. *Acta Metall.* 33 (8), 1481–1488. [http://dx.doi.org/10.1016/0001-6160\(85\)90049-5](http://dx.doi.org/10.1016/0001-6160(85)90049-5).
- Roters, F., Eisenlohr, P., Hantcherli, L., Tjahjanto, D.D., Bieler, T.R., Raabe, D., 2010. Overview of constitutive laws, kinematics, homogenization, and multiscale methods in crystal plasticity finite element modeling: theory, experiments, applications. *Acta Mater.* 58, 1152–1211. <http://dx.doi.org/10.1016/j.actamat.2009.10.058>.
- Roters, F., Eisenlohr, P., Kords, C., Tjahjanto, D.D., Diehl, M., Raabe, D., 2012. DAMASK: the Düsseldorf advanced material simulation kit for studying crystal plasticity using an FE based or a spectral numerical solver. In: Cazacu, O. (Ed.), *Procedia IUTAM: IUTAM Symposium on Linking Scales in Computation: from Microstructure to Macroscale Properties*, vol. 3. Elsevier, Amsterdam, pp. 3–10. <http://dx.doi.org/10.1016/j.piutam.2012.03.001>.
- Sachs, G., 1929. *Mitteilungen der deutschen Materialprüfungsanstalten*, chapter Zur Ableitung einer Fließbedingung, pp. 94–97. http://dx.doi.org/10.1007/978-3-642-92045-5_12.
- Sachtleber, M., Zhao, Z., Raabe, D., 2002. Experimental investigation of plastic grain interaction. *Mater. Sci. Eng. A* 336 (1–2), 81–87. [http://dx.doi.org/10.1016/S0921-5093\(01\)01974-8](http://dx.doi.org/10.1016/S0921-5093(01)01974-8).
- Savoie, M.J., MacEwen, S.R., 1996. A sixth order inverse potential function for incorporation of crystallographic texture into predictions of properties of aluminium sheet. *Text. Microstruct.* 26–27, 495–512.
- Segurado, J., Lebensohn, R.A., Llorca, J., Tomé, C.N., 2012. Multiscale modeling of plasticity based on embedding the viscoplastic self-consistent formulation in implicit finite elements. *Int. J. Plast.* 28 (1), 124–140. <http://dx.doi.org/10.1016/j.ijplas.2011.07.002>.
- Shanthraj, P., Eisenlohr, P., Diehl, M., Roters, F., 2015. Numerically robust spectral methods for crystal plasticity simulations of heterogeneous materials. *Int. J. Plast.* 66, 31–45. <http://dx.doi.org/10.1016/j.ijplas.2014.02.006>.
- Tasan, C.C., Diehl, M., Yan, D., Zambaldi, C., Shanthraj, P., Roters, F., Raabe, D., 2014a. Integrated experimental-numerical analysis of stress and strain partitioning in multi-phase alloys. *Acta Mater.* 81, 386–400. <http://dx.doi.org/10.1016/j.actamat.2014.07.071>.
- Tasan, C.C., Hoefnagels, J.P.M., Diehl, M., Yan, D., Roters, F., Raabe, D., 2014b. Strain localization and damage in dual phase steels investigated by coupled in-situ deformation experiments-crystal plasticity simulations. *Int. J. Plast.* 63, 198–210. <http://dx.doi.org/10.1016/j.ijplas.2014.06.004>.
- Taylor, G.I., 1938. Plastic strain in metals. *J. Inst. Metals* 62, 307–324.
- Tjahjanto, D.D., Eisenlohr, P., Roters, F., 2010. A novel grain cluster-based homogenization scheme. *Model. Simul. Mater. Sci. Eng.* 18 (015006) <http://dx.doi.org/10.1088/0965-0393/18/1/015006>.
- Van Houtte, P., 1994. Application of plastic potentials to strain rate sensitive and insensitive anisotropic materials. *Int. J. Plast.* 10 (7), 719–748. [http://dx.doi.org/10.1016/0749-6419\(94\)90043-4](http://dx.doi.org/10.1016/0749-6419(94)90043-4).
- Van Houtte, P., Delannay, L., Samajdar, I., 1999. Quantitative prediction of cold rolling textures in low-carbon steel by means of the Lamel model. *Text. Microstruct.* 31 (3), 109–149. <http://dx.doi.org/10.1155/TSM.31.109>.
- Van Houtte, P., 2001. Fast calculation of average Taylor factors and Mandel spins for all possible strain modes. *Int. J. Plast.* 17 (6), 807–818. [http://dx.doi.org/10.1016/S0749-6419\(00\)00069-3](http://dx.doi.org/10.1016/S0749-6419(00)00069-3).
- Van Houtte, P., Delannay, L., Kalidindi, S.R., 2002. Comparison of two grain interaction models for polycrystal plasticity and deformation texture prediction. *Int. J. Plast.* 18 (3), 359–377. [http://dx.doi.org/10.1016/S0749-6419\(00\)00102-9](http://dx.doi.org/10.1016/S0749-6419(00)00102-9).
- Van Houtte, P., Van Bael, A., 2004. Convex plastic potentials of fourth and sixth rank for anisotropic materials. *Int. J. Plast.* 20 (8–9), 1505–1524. <http://dx.doi.org/10.1016/j.ijplas.2003.11.005>.
- Van Houtte, P., Li, S., Seefeldt, M., Delannay, L., 2005. Deformation texture prediction: from the Taylor model to the advanced Lamel model. *Int. J. Plast.* 21 (3), 589–624. <http://dx.doi.org/10.1016/j.ijplas.2004.04.011>.
- Van Houtte, P., Yerra, S.K., Van Bael, A., 2009. The facet method: a hierarchical multilevel modelling scheme for anisotropic convex plastic potentials. *Int. J. Plast.* 25, 323–360. <http://dx.doi.org/10.1016/j.ijplas.2008.02.001>.
- Van Houtte, P., Gawad, J., Eyckens, P., Van Bael, B., Samaey, G., Roose, D., 2011. A full-field strategy to take texture-induced anisotropy into account during FE simulations of metal forming processes. *JOM* 63 (11), 37–43. <http://dx.doi.org/10.1007/s11837-011-0189-9>.
- von Mises, R., 1928. *Mechanik der plastischen Formänderung von Kristallen*. *ZAMM Z. Angew. Math. Mech.* 8 (3), 161–185. <http://dx.doi.org/10.1002/zamm.19280080302>.
- Wang, H., Wan, M., Wu, X., Wu, Y., 2009. The equivalent plastic strain-dependent Yld2000-2d yield function and the experimental verification. *Comput. Mater. Sci.* 47 (1), 12–22. <http://dx.doi.org/10.1016/j.commatsci.2009.06.008>.

- Woodthorpe, J., Pearce, R., 1970. The anomalous behaviour of aluminium sheet under balanced biaxial tension. *Int. J. Mech. Sci.* 12 (4), 341–347. [http://dx.doi.org/10.1016/0020-7403\(70\)90087-1](http://dx.doi.org/10.1016/0020-7403(70)90087-1).
- Wu, P.D., Neale, K.W., Van Der Giessen, E., Jain, M., MacEwen, S.R., Makinde, A., 1998. Crystal plasticity forming limit diagram analysis of rolled aluminum sheets. *Metall. Mater. Trans. A* 29 (2), 527–535. <http://dx.doi.org/10.1007/s11661-998-0134-x>.
- Wu, P.D., Jain, M., Savoie, J., MacEwen, S.R., Tuğcu, P., Neale, K.W., 2003. Evaluation of anisotropic yield functions for aluminum sheets. *Int. J. Plast.* 19 (1), 121–138. [http://dx.doi.org/10.1016/S0749-6419\(01\)00033-X](http://dx.doi.org/10.1016/S0749-6419(01)00033-X).
- Yoon, J.W., Barlat, F., Dick, R.E., Chung, K., Kang, T.J., 2004. Plane stress yield function for aluminum alloy sheets-part II: FE formulation and its implementation. *Int. J. Plast.* 20 (3), 495–522. [http://dx.doi.org/10.1016/S0749-6419\(03\)00099-8](http://dx.doi.org/10.1016/S0749-6419(03)00099-8).
- Yoon, J.W., Barlat, F., Dick, R.E., Karabin, M.E., 2006. Prediction of six or eight ears in a drawn cup based on a new anisotropic yield function. *Int. J. Plast.* 22 (1), 174–193. <http://dx.doi.org/10.1016/j.ijplas.2005.03.013>.
- Yoon, J.W., Lou, Y., Yoon, J., Glazoff, M.V., 2014. Asymmetric yield function based on the stress invariants for pressure sensitive metals. *Int. J. Plast.* 56, 184–202. <http://dx.doi.org/10.1016/j.ijplas.2013.11.008>.
- Zeman, J., Vondřejc, J., Novák, J., Marek, I., 2010. Accelerating a FFT-based solver for numerical homogenization of periodic media by conjugate gradients. *J. Comput. Phys.* 229 (21), 8065–8071. <http://dx.doi.org/10.1016/j.jcp.2010.07.010>.
- Zhang, K., Holmedal, B., Hopperstad, O.S., Dumoulin, S., 2014. Modelling the plastic anisotropy of aluminum alloy 3103 sheets by polycrystal plasticity. *Model. Simul. Mater. Sci. Eng.* 22 (7), 075015. <http://dx.doi.org/10.1088/0965-0393/22/7/075015>.
- Zhang, C., Li, H., Eisenlohr, P., Liu, W.J., Boehlert, C.J., Crimp, M.A., Bieler, T.R., 2015a. Effect of realistic 3D microstructure in crystal plasticity finite element analysis of polycrystalline Ti-5Al-2.5Sn. *Int. J. Plast.* 69, 21–35. <http://dx.doi.org/10.1016/j.ijplas.2015.01.003>.
- Zhang, K., Holmedal, B., Hopperstad, O.S., Dumoulin, S., Gawad, J., Bael, A.V., Houtte, P.V., 2015b. Multi-level modelling of mechanical anisotropy of commercial pure aluminium plate: crystal plasticity models, advanced yield functions and parameter identification. *Int. J. Plast.* 66, 3–30. <http://dx.doi.org/10.1016/j.ijplas.2014.02.003>.
- Zhao, P., Wang, Q., Zhai, C., Zhu, Y., 2007. Effects of strontium and titanium on the microstructure, tensile properties and creep behavior of AM50 alloys. *Mater. Sci. Eng. A* 444 (1–2), 318–326. <http://dx.doi.org/10.1016/j.msea.2006.08.111>.
- Zhao, Z., Ramesh, M., Raabe, D., Cuitiño, A.M., Radovitzky, R., 2008. Investigation of three-dimensional aspects of grain-scale plastic surface deformation of an aluminum oligocrystal. *Int. J. Plast.* 24, 2278–2297. <http://dx.doi.org/10.1016/j.ijplas.2008.01.002>.